eprints@whiterose.ac.uk
https://eprints.whiterose.ac.uk/

Outflow densities and ionization mechanisms in the NLRs of the prototypical Seyfert galaxies NGC 1068 and NGC 4151

Luke R. Holden ⭐ and Clive N. Tadhunter

Department of Physics & Astronomy, University of Sheffield, S6 3TG Sheffield, UK

ABSTRACT

Despite being thought to play an important role in galaxy evolution, the true impact of outflows driven by active galactic nuclei (AGNs) on their host galaxies is unclear. In part, this may be because electron densities of outflowing gas are often underestimated: recent studies that use alternative diagnostics have measured much higher densities than those from commonly used techniques and consequently find modest outflow masses and kinetic powers. Furthermore, outflow ionization mechanisms – which are often used to probe acceleration mechanisms – are also uncertain. To address these issues, we have analysed archival HST/STIS spectra of the inner regions (r < 160 pc) of the nearby prototypical Seyfert galaxies NGC 1068 and NGC 4151, which show evidence of warm-ionized outflows driven by the central AGN. We derive high electron densities ($10^{3.6} < n_e < 10^{4.8}$ cm^{-3}) using the transauroral [O II] and [S II] emission line ratios for the first time with spatially resolved observations. Moreover, we find evidence that the gas along the radio axis in NGC 1068 has a significant AGN-photoionized matter-bounded component, and there is evidence for shock-ionization and/or radiation-bounded AGN-photoionization along the radio axis in NGC 4151. We also note that the outflow extents are similar to those of the radio structures, consistent with acceleration by jet-induced shocks. Taken together, our investigation demonstrates the diversity of physical and ionization conditions in the narrow-line regions of Seyfert galaxies, and hence reinforces the need for robust diagnostics of outflowing gas densities and ionization mechanisms.

Key words: galaxies: active – galaxies: evolution – galaxies: individual: NGC 4151 – galaxies: individual: NGC 1068 – galaxies: Seyfert – ISM: jets and outflows.

1 INTRODUCTION

Active galactic nuclei (AGNs) can drive gas outflows through radiation-pressure-driven winds from their accretion discs (Di Matteo, Springel & Hernquist 2005; Hopkins & Elvis 2010) and/or radio jets (Axon et al. 1998; Wagner & Bicknell 2011; Mukherjee et al. 2018). These outflows, as well as the heating and ionizing of near-nuclear gas, may constitute an important part of 'AGN feedback', which now routinely plays a crucial role in theoretical models of galaxy evolution. AGN-feedback is required to explain observed galaxy properties (e.g. Di Matteo et al. 2005; Somerville et al. 2008; Schaye et al. 2015; Dubois et al. 2016; Davé et al. 2019) and empirical scaling relations between super massive black holes and host galaxy properties (e.g. Magorrian et al. 1998; Silk & Rees 1998; Fabian 1999; Ferrarese & Merritt 2000; Gebhardt et al. 2000). Models often require that the kinetic power ($\dot{E}_{kin}$) of the outflowing gas is above a certain fraction of the AGN bolometric luminosity (L_{bol}): this is characterized by a ratio known as the 'coupling factor' ($\epsilon_f = \dot{E}_{kin}/L_{bol}$) and is typically required to be in the range $0.5 < \epsilon_f < 10$ per cent (Di Matteo et al. 2005; Springel, Di Matteo & Hernquist 2005; Hopkins & Elvis 2010).

Observational studies commonly attempt to quantify the impact of outflows on their host galaxies by comparing measured coupling efficiencies to those required by models (e.g. Liu et al. 2013; Cicone

et al. 2014; Harrison et al. 2014; Rose et al. 2018; Riffel 2021). However, many key outflow properties are highly uncertain, leading to a wide range of observationally-derived coupling efficiencies (Harrison et al. 2018). For the warm ionized outflow phase (i.e. traced by [O III] and Hβ; $10\,000 < T_e < 25\,000$ K), the largest source of uncertainty is likely to be the electron density of the outflowing gas, which is often estimated or assumed to be relatively low: in the range $n_e \sim 100$–1000 cm^{-3} (e.g. Kraemer & Crenshaw 2000a; Nesvadba et al. 2006; Fiore et al. 2017). This may be because the commonly used 'traditional' density diagnostics – the [S II](6717/6731) and [O II](3726/3729) emission-line doublet ratios – are only sensitive up to $n_e \sim 10^{3.5}$ cm^{-3}, and are often blended due to complex outflow kinematics. However, in recent years, alternative density diagnostics have been developed and used, such as detailed photoionization modelling that makes use of a wide range of emission lines (Collins et al. 2009; Crenshaw et al. 2015; Revalski et al. 2021, 2022), and a technique that involves combining ionization parameter measurements with infrared estimates of outflow radii (Baron & Netzer 2019). Such methods have measured higher electron densities for the warm ionized phase than commonly-used traditional techniques, up to $n_e \sim 10^{5.5}$ cm^{-3}. Moreover, studies that make use of the higher critical density 'transauroral' ('TR'; Boyce, Menzel & Payne 1933) [O II](3726 + 3729)/(7319 + 7331) and [S II](4068 + 4076)/(6717 + 6731) diagnostic ratios have similarly found densities in the range of $10^3 < n_e < 10^{5.5}$ cm^{-3} (Holt et al. 2011; Rose et al. 2018; Santoro et al. 2018, 2020; Spence et al. 2018; Ramos Almeida et al. 2019;

⭐ E-mail: lholden2@sheffield.ac.uk

Davies et al. 2020; Speranza et al. 2022; Holden et al. 2023). Considering that the derived outflow kinetic power is inversely proportional to the electron density, if electron densities are truly orders of magnitude higher than are commonly assumed or estimated, the resulting kinetic powers and coupling factors for the warm ionized phase will be orders of magnitude lower. This could significantly change our understanding of the importance of AGN feedback in galaxy evolution.

Moreover, where possible, it is important to use spatially-resolved observations when deriving electron densities, since global electron densities may significantly underestimate the values at small radial distances from the nucleus, where the outflows are the most extreme (Revalski et al. 2022; but see also Kakkad et al. 2018). Thus, detailed spatially-resolved observations are needed to robustly assess electron densities in different types of AGN as well as to compare and verify different density diagnostics.

Investigations into the impact of outflows on their host galaxies are further complicated by the fact that the dominant acceleration and ionization mechanisms are unclear: while it is thought that outflows may be accelerated by radiation pressure from the AGN (either '*in situ*'; e.g. Crenshaw et al. 2015; Fischer et al. 2017; Revalski et al. 2018; Meena et al. 2023, or from the nucleus: e.g. Hopkins & Elvis 2010; Meena et al. 2021), a study of a large sample of local AGN found a link between intermediate radio power AGN ($L_{1.4\,GHz} = 10^{23-25}\,W\,Hz^{-1}$) and outflow kinematics (Mullaney et al. 2013), suggesting that feedback from jets is also important in AGN that are classified as radio quiet. Indeed, hydrodynamic simulations have shown that jets interacting with the ISM on kpc-scales can explain observed gas kinematics in some objects (e.g. Mukherjee et al. 2018; Audibert et al. 2023) and may have both a positive and negative impact on local star formation rates (Mandal et al. 2021). Therefore, determining dominant acceleration mechanisms is crucial for making proper comparisons between observations and predictions from theoretical modelling, which are needed to interpret the role of outflows in an AGN feedback.

The ionization and excitation mechanisms of the outflowing gas may provide clues as to the acceleration mechanism(s) present. For example, shock-ionized gas must have passed through (and been accelerated by) a shock. However, AGN-photoionized gas may have been previously accelerated by another mechanism and reionized by photons from the AGN after cooling (Holden et al. 2023). Hence, the true nature of the relationship between outflow acceleration and ionization mechanisms is complex and requires further careful analysis.

Regardless of how outflows are accelerated, understanding the dominant ionization mechanisms impacts our ability to extract key diagnostic information for the warm outflowing gas. Specifically, the techniques presented by Holt et al. (2011) and Revalski et al. (2021; see also Collins et al. 2009) both rely on photoionization models, and the TR lines (in the case of the Holt et al. 2011 method) cannot be emitted by a matter-bounded component. If, in reality, a gas outflow is shock-ionized or has a large contribution from a matter-bounded component, this may have a significant impact on the validity of these methods. Thus, it is important to investigate the potential impact of matter-bounded components or shock ionization on derived densities.

In order to address these issues, we are undertaking spatially resolved studies of nearby AGN that show clear evidence of outflows on pc to kpc scales. In Holden et al. (2023), we presented a detailed study of the central regions of the nearby Seyfert 2 IC 5063 using Very Large Telescope (VLT)/Xshooter ultraviolet (UV), optical, and near-infrared (NIR) spectroscopy. We found electron densities

just above the critical density of the traditional [S II] ratio, and evidence for a post-shock cooling sequence and reionization via AGN photoionization.

There is a clear need to determine whether the conditions found in the narrow-line region (NLR) of IC 5063 are similar in other Seyfert galaxies, specifically to further investigate the true outflow gas density, kinetic powers, and ionization mechanisms present on different spatial scales. Therefore, here we analyse archival Hubble Space Telescope (HST)/Space Telescope Imaging Spectrograph (STIS) spectra of the inner NLRs ($r < 160\,kpc$) of the prototypical Seyfert galaxies NGC 1068 and NGC 4151, and apply and expand upon many of the techniques presented in Holden et al. (2023). We take the distances to NGC 1068 and NGC 4151 to be $D = 13.0\,Mpc$ (Revalski et al. 2021) and $D = 15.8\,Mpc$ (Yuan et al. 2020), respectively, which correspond to spatial scales of $0.067\,kpc\,arcsec^{-1}$ for NGC 1068 and $0.078\,kpc\,arcsec^{-1}$ for NGC 4151.

The structure of the paper is as follows: in Section 2, we introduce the prototypical Seyfert galaxies NGC 1068 and NGC 4151; in Section 3, we detail the archival HST/STIS observations and our data reduction and handling processes; in Section 4, we present our analysis of the STIS data; in Section 5, we discuss the implications of our findings, and in Section 6, we give our conclusions.

2 TWO PROTOTYPICAL SEYFERTS: NGC 1068 AND NGC 4151

NGC 1068 and NGC 4151 appeared in Carl Seyfert's original paper that established the Seyfert class (Seyfert 1943) and are respectively the prototypical Seyfert 2 (Sey2) and Seyfert 1 (Sey1) galaxies. In consequence, they are perhaps the most well-studied AGN of their respective types. Their close proximity to Earth, and the previous, extensive multi-wavelength studies of their properties, make them ideal objects for our project: the outflows in their central regions can be spatially resolved, and we can compare our results to those obtained using other methods. Principally, this allows us to assess the validity of the different density diagnostic techniques as well as investigate the ionization of the gas.

2.1 NGC 1068

NGC 1068 is one of the closest and brightest (in terms of observed flux) Seyfert 2 galaxies, allowing detailed spatially-resolved observations, and thus making it the target for extensive studies that cover a range of spatial scales in the optical (e.g. Cecil, Bland & Tully 1990; Evans et al. 1991; Axon et al. 1998; Crenshaw & Kraemer 2000b; Kraemer & Crenshaw 2000b; Das et al. 2006), NIR (e.g. Müller Sánchez et al. 2009; Raban et al. 2009; May & Steiner 2017), and radio (e.g. Wilson & Ulvestad 1983; Gallimore et al. 1996; García-Burillo et al. 2014, 2019). NGC 1068 has a radio luminosity of $L_{1.4\,GHz} = 2.3 \times 10^{23}\,W\,Hz^{-1}$ (Ulvestad & Wilson 1984), placing it in the upper end of the radio luminosity range for Seyfert galaxies, and its high bolometric luminosity ($0.4 < L_{bol} < 4.7 \times 10^{38}\,W$: Woo & Urry 2002; Alonso-Herrero et al. 2011; Lopez-Rodriguez et al. 2018; Gravity Collaboration 2020) is close to the lower boundary of the luminosity range for quasars ($L_{bol} > 10^{38}\,W$). The galaxy also has an important historical role, as it was the first object used to verify the orientation-based unified scheme for AGN (Antonucci & Miller 1985).

The NLR of NGC 1068 presents as an 'hourglass'-shaped bicone (Barbosa et al. 2014; Riffel et al. 2014; May & Steiner 2017) with an opening angle of $\theta \sim 40°$ along $PA = 30 \pm 2°$ at an inclination of $i = 5°$, placing the bicone axis close to the plane of the sky and
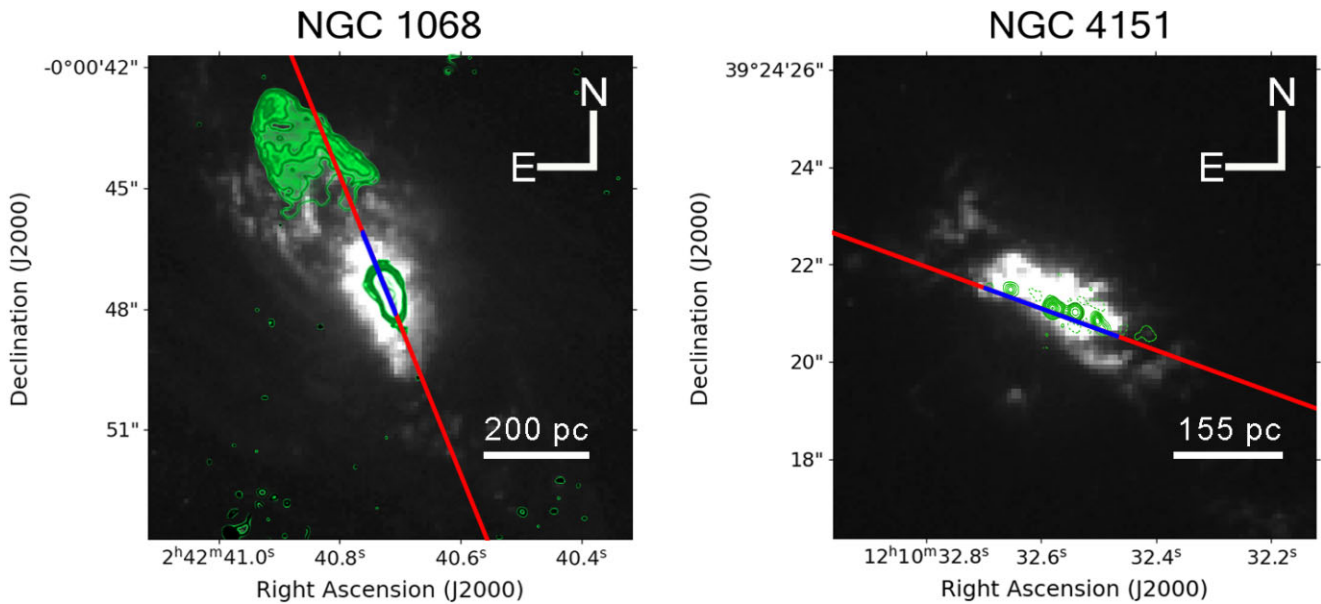
Figure 1. The STIS slits of our archival observations (red) shown plotted over archival HST/WFPC2 [O III] emission-line images of the inner regions of NGC 1068 and NGC 4151, taken with the F502N filter (NGC 1068: GTO:5754, PI Ford; NGC 4151: GTO:5124; PI Ford). The extents of our apertures (Section 3.2.2) along the slits are shown in blue. *Left:* The STIS slit shown over the [O III] emission-line image of the near-nuclear regions of NGC 1068. VLA 22 GHz contours from Gallimore et al. (1996) are presented in green, showing the radio structure near the core and an extended lobe to the NE. *Right:* the STIS slit shown over the [O III] emission-line image of the near-nuclear regions of NGC 4151; the green contours are from high-resolution eMERLIN 1.5 GHz imaging presented by Williams et al. (2017) and show a string of radio knots near the nucleus. We note that, while the narrow-band images are not continuum-subtracted, the brighter parts of the NLR emission are dominated by [O III] emission in the filter bandpass, so the images provide a good representation of the main NLR structures.

inclined $\sim 45°$ out of the galaxy's disc (Das et al. 2006; but see also Crenshaw & Kraemer 2000b). Outflows of warm-ionized gas with velocities up to ~ 1500 km s^{-1} have been detected in the bicone (Crenshaw & Kraemer 2000b; Das et al. 2006). In the northeast (NE) cone, the radio axis is closely aligned with the bicone axis – interpreted as a radio jet propagating within the hollowed-out cone – with a radio lobe that extends just beyond the maximum extent of the cone (Wilson & Ulvestad 1987; shown in Fig. 1). Lower velocity cold molecular CO(3–2) outflows have been detected at this position, indicating that the lobe may represent the termination of the AGN-driven outflows (García-Burillo et al. 2014).

The outflows in the NLR of NGC 1068 have been argued to be radiatively accelerated by some authors (Kraemer & Crenshaw 2000b; Das et al. 2006; Revalski et al. 2021; Meena et al. 2023), while others have proposed they are driven by jet-induced shocks (Capetti, Macchetto & Lattanzi 1997; Axon et al. 1998). May & Steiner (2017) propose a scenario in which the radio jet impacts molecular clouds on small radial scales near the central AGN, accelerating high-velocity 'bullets' of gas that propagate within the bicone but constitute only a small fraction of the total outflowing mass.

2.2 NGC 4151

NGC 4151 is the prototypical Seyfert 1 (Sey1) galaxy[1] and is also one of the closest and brightest (in terms of observed flux) of its class, leading to its NLR outflows being the target of extensive studies of the coronal (e.g. Storchi-Bergmann et al. 2009, 2010), warm ionized (e.g. Winge et al. 1997; Hutchings et al. 1999; Crenshaw et al. 2000; Das et al. 2005; May et al. 2020), and warm molecular (H$_2$; $T \sim 2000$ K,

[1] NGC 4151 was later classified as an intermediate 'Seyfert 1.5' (Osterbrock & Koski 1976; Robinson et al. 1994).

e.g. May et al. 2020) gas phases, which have distinct flux distributions (Storchi-Bergmann et al. 2009). Similar to NGC 1068, the bicone-shaped NLR also has an hourglass morphology (May et al. 2020), with PA = 22° at an inclination of $i = 21°$ (Pedlar et al. 1992; 36° to the galactic disc) and an opening angle of 33° (Das et al. 2005). However, the bolometric luminosity of the AGN in NGC 4151 ($L_{\rm bol} = 1.4 \times 10^{37}$ W: Kraemer et al. 2020) is approximately an order of magnitude below that of NGC 1068.

The radio source of luminosity $L_{1.4\,\rm GHz} = 1.6 \times 10^{22}$ W Hz^{-1} (Ulvestad & Wilson 1984) consists of a double sided jet (PA $\sim 77°$) originating from the nucleus. High-resolution radio imaging (Carral, Turner & Ho 1990; Pedlar et al. 1993; Williams et al. 2017) shows several radio knots along this structure within the central few arc-seconds, whereas lower-resolution radio observations (Johnston et al. 1982; Pedlar et al. 1993) reveal a larger-scale lower surface brightness structure with a radio lobe in the NE cone extending to 6.3 arcsec from the nucleus along the radio axis. It has been argued that the radio jet has little connection to the NLR outflow kinematics in NGC 4151 (Hutchings et al. 1999; Crenshaw et al. 2000; Das et al. 2005). However, enhanced line fluxes from the warm ionized gas, high electron temperatures ($T_e > 16,000$ K) and high [Fe II]/[P II] ratios have been spatially associated with the radio structure (Mundell et al. 2003; Storchi-Bergmann et al. 2009, 2010), indicating that jet–ISM interactions may still drive shocks into the gas at certain locations within the bicone (see also Wang et al. 2011a, b; Williams et al. 2017).

May et al. (2020) propose a similar model as they proposed for NGC 1068 (May & Steiner 2017) – albeit on smaller spatial scales with less extreme kinematics – to explain the NLR and outflow structure in NGC 4151: the radio jet impacts a molecular cloud near the nucleus (potentially due to misalignment between the jet and torus/disc: Storchi-Bergmann et al. 2010; May et al. 2020), driving fragmented, shock-accelerated gas into the cones and contributing to the NLR morphology.

2.3 Previous photoionization modelling of NGC 1068 and NGC 4151

Crenshaw et al. (2015) and Revalski et al. (2021, 2022) performed detailed, multi-ionization component photoionization modelling of the warm ionized outflows in NGC 1068 and NGC 4151, finding densities in the range $10^{3.0}$ cm^{-3} $< n_e <$ $10^{7.2}$ cm^{-3} for the NLR gas in both objects, and coupling efficiencies above the lower limit required by galaxy evolution models (0.5 per cent: Hopkins & Elvis 2010) in the case of NGC 1068. In order to further investigate the electron densities of the outflowing gas in the NLR of these two important objects, and to attempt to clarify the uncertainties regarding the acceleration and ionization mechanisms of the gas, we require high spatial resolution, wide wavelength-coverage long-slit spectroscopy with the slit aligned along the radio axis (which is approximately along the bicone axes).

3 OBSERVATIONS AND DATA REDUCTION

3.1 Archival HST/STIS observations

To achieve our science goals, suitable archival HST/STIS long-slit spectra were downloaded from the Hubble Legacy Archive (HLA; https://hla.stsci.edu/hlaview.html). We required data taken using both the G430L and G750L gratings in order to ensure sufficient wavelength coverage, namely that the spectra contained the blue [S II] λλ4068, 4076 and red [O II] λλ7319, 7331 transauroral doublets. Both instrument set-ups have a spatial pixel scale of 0.051 arcsec per pixel, and the dispersions of the two gratings are 2.72 Å pixel^{-1} (G430L; 2900–5700 Å) and 4.92 Å pixel^{-1} (G750L; 5240–10 270 Å). We also required that these data were taken along (or close to) the PA of the radio/bicone structures to ensure we are tracing the the gas that is impacted most by the jet. The data for NGC 1068 were taken as part of the Cycle 7 HST Proposal GTO:7573 (PI Kraemer), with a 52 × 0.1 arcsec slit along PA = 202°, centred on a bright emission-line knot close (<0.4 arcsec) to the nucleus (see Crenshaw & Kraemer 2000a and Kraemer & Crenshaw 2000a). Data for NGC 4151 were taken with a 52 × 0.1 arcsec slit along PA = 70°, offset to the south by 0.1 arcsec to reduce contamination from the bright Sey1 nucleus, and were taken in Cycle 7 as part of HST Proposal GTO:7569 (PI Hutchings) – a full description of the NGC 4151 observations is given by Nelson et al. (2000). We show the positions of the STIS slits over the central regions of the two Seyferts in Fig. 1.

3.2 Reduction and handling of STIS data

3.2.1 Data reduction

The first step in the data reduction was performed with the standard CALSTIS pipeline. For the NGC 1068, only a single exposure for each grating was available, while for NGC 4151, we took the average of two exposures for each grating using PYTHON scripts, which made use of the NUMPY (Harris et al. 2020) and ASTROPY (Astropy Collaboration 2013, 2018) modules. In order to ensure that the individual exposures for each grating were aligned, we first extracted spatial slices along the slit direction in a line-free region of the continuum covering the wavelength range 5480–5600 Å for the G430L grating and 6795–6890 Å for the G750L grating. The centroids of the spatial peaks – determined with Gaussian profile fits – were consistent within better than 0.4 pixels, confirming that each exposure was taken with the same telescope pointing within

0.02 arcsec. We also checked that the spectra taken with the G430L and G750L gratings for the each object were aligned using the same method of Gaussian fits to the spatial flux profiles. Again, the spatial positions of the peak flux between gratings were consistent to within better than 0.4 pixels, indicating that the observations with different gratings were closely spatially aligned.

Residual hot pixels and cosmic rays were removed from the spectra using the CLEAN command from the STARLINK FIGARO software package (Currie et al. 2014). We then corrected for extinction due to dust in the Milky Way using the Galactic extinction maps presented by Schlegel, Finkbeiner & Davis (1998) and recalibrated by Schlafly & Finkbeiner (2011). Using the NASA/IPAC Infrared Science Archive reddening lookup tool (https://irsa.ipac.caltech.edu/applications/DUST/) with these maps, we find that there are mean colour excesses in the directions of NGC 1068 and NGC 4151 of E(B–V)$_{mean}$ = 0.0289 ± 0.0004 and E(B–V)$_{mean}$ = 0.0237 ± 0.0011, respectively. The R_v = 3.1 extinction law presented by Cardelli, Clayton & Mathis (1989; hereafter CCM89) was then used to correct for Galactic extinction.

3.2.2 Aperture selection and extraction

The STIS long-slit spectra of NGC 1068 and NGC 4151 show disturbed kinematics (indicating outflows) and several bright emission-line knots in the central few hundred parsecs, as noted by previous studies (Kraemer & Crenshaw 2000a; Crenshaw & Kraemer 2000b; Das et al. 2005, 2006; Meena et al. 2023). We extracted several apertures (integrated groupings of pixel rows) from the 2D G430L and G750L spectra, with each aperture forming an integrated 1D spectrum that corresponds to a certain spatial position along the slit. We selected the apertures to cover the locations of the bright emission knots seen in our 2D spectra (Fig. 2). The widths of the apertures (6–15 pixels; 0.3–0.8 arcsec) were set to contain sufficient signal in the fainter emission lines that are used for diagnostics in our analysis, namely the fainter TR [O II] λλ7319,7331 and [S II] λλ4068,4076 doublets. We extracted the same apertures from the G430L and G750L spectra for each object, as we previously determined that the spectra were closely spatially aligned (Section 3.2.1). Flux errors were determined by adding the flux errors from individual pixel rows (which constitute a given aperture) in quadrature. As an example, we present part of the spectrum of aperture 2 for NGC 1068 in Fig. 3. The chosen apertures extended out to a maximum radial distance of 139 pc for NGC 1068 and 151 pc in the case of NGC 4151.

Aperture 3 for NGC 1068 was placed over a bright emission knot that corresponds to a previously detected radio source at the likely position of the galaxy's nucleus (see discussion in Kraemer & Crenshaw 2000a), while Aperture 4 for NGC 4151 corresponds to the location along the slit that is closest to the nucleus. We note that the spectra for NGC 4151 do not directly cover the nucleus due to the 0.1 arcsec slit offset to the south to avoid nuclear contamination. Unfortunately, the south-west part of the slit for NGC 1068 (seen above Aperture 4 in Fig. 2) did not contain enough signal for the measurement of the faint [O II] λλ7319, 7331 TR doublet, even when integrated as a single aperture. Therefore, we omit this region from our analysis.

Following aperture extraction, we ensured that the flux calibration was consistent between the two gratings for each aperture by overplotting the spectra in the region where the wavelength ranges of the gratings overlap (5275–5705 Å). We found that all apertures for NGC 1068 are closely matched in flux. However, for apertures 2 and 4 of NGC 4151, the flux in the overlap region was >8 per cent
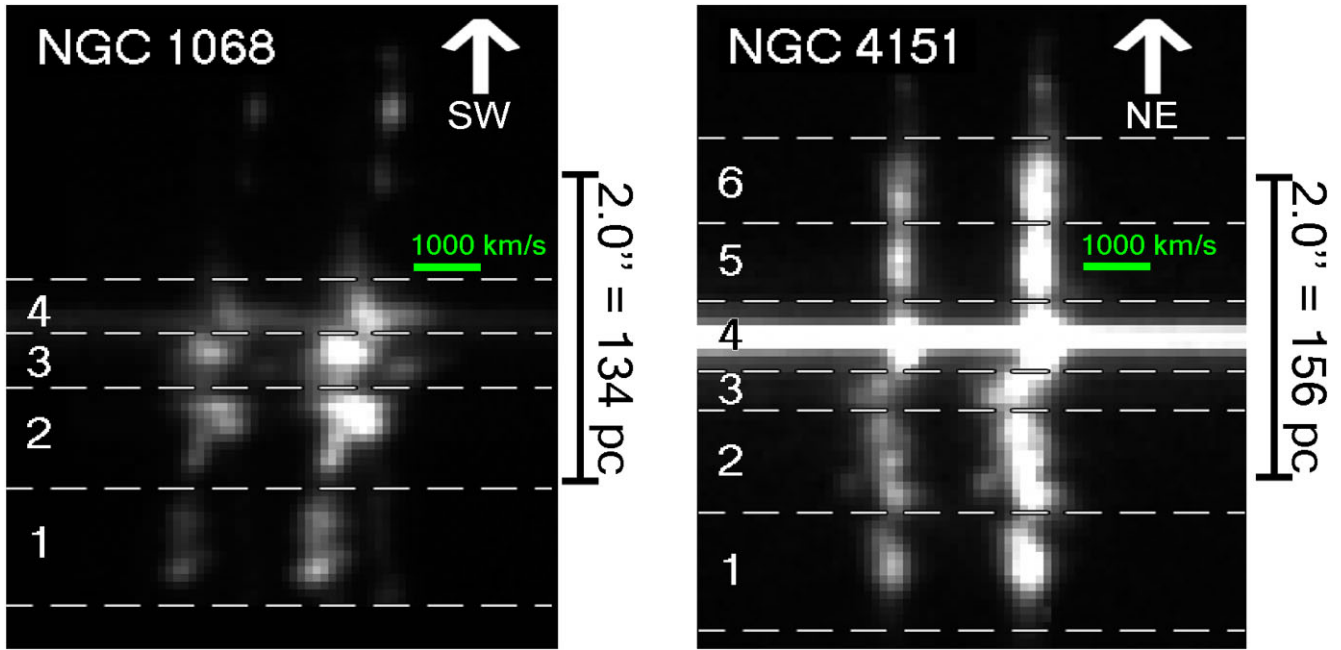
Figure 2. Selected apertures for NGC 1068 (left) and NGC 4151 (right), positioned over the [O III] λλ4959,5007 doublet in the 2D STIS G430L spectra. The spectral direction is horizontal (left = bluewards; right = redwards) and the vertical direction is spatial along the slit (with the direction shown by the labelled arrows); velocity scale bars are shown in green, and the spatial extents in arcsec and parsecs are shown to the right of each spectrum. The apertures are shown as regions bounded by dashed lines and are labelled on the left of each image – they were chosen to contain enough signal for the measurement of faint lines in distinct kinematic regions within the central few hundred parsecs of each galaxy.
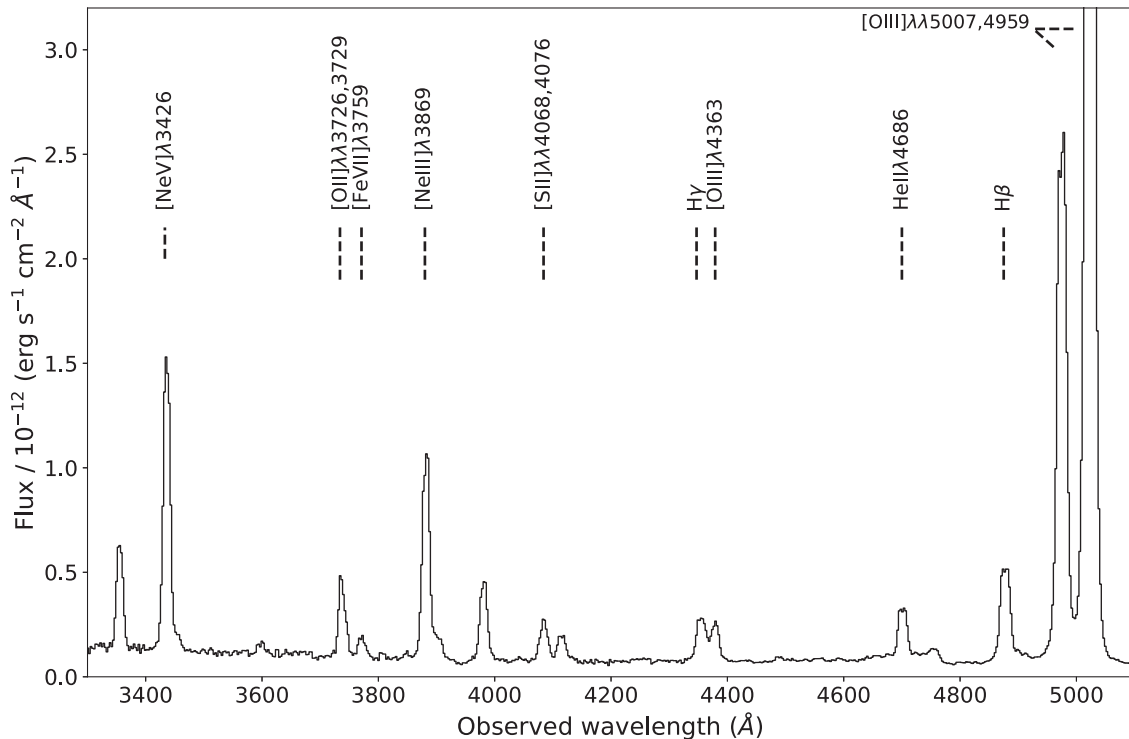

Figure 3. The G430L grating spectrum for Aperture 2 of NGC 1068 (Fig. 2). Key emission lines that are used in our analysis are labelled with dotted lines. Note that, for presentation reasons, the limit on the flux axis has been chosen so that fainter lines can be clearly seen; as a result, the peak of the [O III] λ5007 line is not visible.

Table 1. [O III] model parameters (galaxy rest-frame component velocity shift: v_c; instrumentally corrected component velocity width: FWHM$_c$), distances from the nucleus (in arcsec and pc), electron densities, reddening values, and electron temperatures for each of our apertures for NGC 1068 and NGC 4151. In apertures where there are multiple Gaussian components for the [O III] models, we label the kinematic parameters for the two components with the subscripts 'a' and 'b'. The densities and reddenings were determined simultaneously using the transauroral line technique (Section 4.1; Fig. 4), and the temperatures were determined using the [O III](5007 + 4959)/4363 ratio (Section 4.2.1).

Aperture	Distance (arcsec)	Distance (pc)	$v_{c, a}$ (km s^{-1})	FWHM$_{c, a}$ (km s^{-1})	$v_{c, b}$ (km s^{-1})	FWHM$_{c, b}$ (km s^{-1})	$\log_{10}(n_e[\text{cm}^{-3}])$	E(B-V)$_{TR}$	T_e (K)
				NGC 1068					
1	− 1.45	− 97	− 828 ± 4	572 ± 25	295 ± 40	1078 ± 96	$4.06^{+0.05}_{-0.06}$	$0.16^{+0.04}_{-0.05}$	$14\,300^{+2100}_{-1300}$
2	− 0.74	− 50	− 184 ± 7	1017 ± 31	–	–	$4.65^{+0.05}_{-0.04}$	$0.05^{+0.04}_{-0.05}$	$14\,400^{+1500}_{-1100}$
3	− 0.23	− 15	− 306 ± 3	662 ± 26	− 5 ± 20	1770 ± 43	$4.74^{+0.05}_{-0.05}$	$0.16^{+0.05}_{-0.04}$	$16\,100^{+1400}_{-1000}$
4	0.10	7	95 ± 3	367 ± 26	235 ± 8	1684 ± 34	$4.45^{+0.09}_{-0.09}$	$0.17^{+0.08}_{-0.08}$	$16\,000^{+1600}_{-1100}$
				NGC 4151					
1	− 1.58	− 123	− 172 ± 2	420 ± 25	− 263 ± 29	1261 ± 102	$3.68^{+0.08}_{-0.10}$	$0.11^{+0.05}_{-0.07}$	$16\,300^{+3400}_{-1800}$
3	− 0.38	− 30	− 392 ± 6	0 ± 28 [a]	− 356 ± 3	1065 ± 26	$4.04^{+0.07}_{-0.15}$	$0.13^{+0.05}_{-0.06}$	$21\,000^{+3300}_{-2100}$
5	0.48	37	34 ± 1	234 ± 24	121 ± 11	1013 ± 44	$3.94^{+0.10}_{-0.10}$	$0.15^{+0.08}_{-0.08}$	$17\,300^{+5200}_{-2400}$
6	1.02	80	40 ± 1	307 ± 25	126 ± 8	768 ± 35	$3.75^{+0.8}_{-0.10}$	$0.23^{+0.07}_{-0.07}$	$15\,200^{+3400}_{-1800}$

[a] The measured width of the *component* is consistent with the instrumental width, and hence unresolved.

higher in the G430L grating than the G750L grating, potentially due to internal reflections within the instrument caused by the bright Type 1 nucleus (see Nelson et al. 2000). Therefore, we do not use these apertures in further analysis.

3.2.3 The contribution of stellar continua to the spectra

We did not model and subtract the underlying stellar continuum in detail using a template-fitting approach (as was done for similar analyses of other objects by Rose et al. 2018 and Holden et al. 2023) for various reasons. First, our archival STIS G430L and G750L spectra did not have sufficient spectral resolution to clearly resolve absorption features that could be used to verify the robustness of the continuum fits. Secondly, there may be substantial contamination by direct and scattered AGN continuum (Antonucci & Miller 1985) and nebular continuum (Tadhunter 2016) that precludes accurate stellar continuum modelling. Finally, the emission lines in our spectra have relatively high equivalent widths (EWs), which fill in various stellar absorption features.

In order to verify whether stellar continuum modelling was needed in this study, we measured the EWs for the Hβ recombination emission line. We find 36 < EW < 148 Å in our NGC 1068 apertures and 30 < EW < 151 Å in the NGC 4151 apertures. The lowest emission-line EW we measure (EW=30 Å for Aperture 3 in NGC 4151) is a factor of three higher than that of the Hβ absorption feature as modelled for a ~400 Myr old stellar population (which gives the highest EWs in modelling by González Delgado, Leitherer & Heckman 1999). Thus, underlying stellar absorption features may affect our measured Hβ luminosities by a maximum factor of 1.3 (for a stellar EW=10 Å). However, this is very much an upper limit since we do not detect a Balmer break in the continuum in any of our apertures, as would be expected for intermediate age stellar populations that have strong Balmer absorption lines.

3.2.4 Fits to key emission lines

The NLR kinematics in NGC 1068 and NGC 4151 are complex, and have been previously modelled in detail as biconical outflows based on higher resolution STIS spectra than those used here (Das et al. 2006 and Das et al. 2005, respectively; but see also Crenshaw &

Kraemer 2000b and Crenshaw et al. 2000). In those studies, the [O III] λλ4959,5007 doublet line profiles were fit with multiple Gaussians for each pixel row of the 2D spectra. Here, we perform a similar procedure for our extracted apertures by simultaneously fitting a first- or second-order polynomial to the continuum surrounding the [O III] λλ4959,5007 doublet, and one or two Gaussian profiles to each of the lines in the doublet itself. We set the wavelength separation of the lines in the doublet, as well as the intensity ratio of the lines (1:2.99), to those defined by atomic physics (Osterbrock & Ferland 2006). Furthermore, we constrained the widths of a given Gaussian component to be the same for each line in the doublet. We present the model parameters for each aperture in Table 1.

Once we had established [O III] λλ4959,5007 doublet fits in each aperture, we calculated the difference between the mean wavelength of each Gaussian component and the rest [O III] wavelength in the reference frame of the galaxy, using redshifts[2] of $z = 0.00381$ for NGC 1068 and $z = 0.003262$ for NGC 4151. We also determined the intrinsic width of each component by subtracting the instrumental width of the STIS G430L grating in quadrature from the measured widths. According to the STIS manual, for a slit of width 0.1 arcsec, the instrumental broadening in the spectral direction is in the range 2 < full width at half-maximum (FWHM) < 3 pixels, corresponding to 5.5 < FWHM < 8.2 Å for the G430L grating and 9.8 < FWHM < 14.8 Å for the G750L grating. By fitting single Gaussians to the [O III] λλ4959,5007 emission-line doublet at a radial distance of 4 arcsec from the nucleus of NGC 4151 in the G430L spectra (where the lowest line widths are measured), we measure a line width of FWHM$_{inst}$ = 6.0 ± 0.4 Å; similarly, measuring the [S II] λ9531 line in the G750L spectra with this method resulted in a line width of FWHM$_{inst}$ = 12.3 ± 2.4 Å. Thus, we adopt instrumental widths of FWHM$_{inst}$ = 6.0 Å (360 km s^{-1} at 5007 Å) and FWHM$_{inst}$ = 12.3 Å (560 km s^{-1} at 6575 Å) for the G430L and G750L gratings, respectively.

In subsequent analysis, we only consider *total* line fluxes – including all Gaussians components used – rather than fluxes from individual components (i.e. potentially representing outflowing and

[2]21 cm redshifts from the NASA/IPAC Extragalactic Database (https://ned.ipac.caltech.edu/).

quiescent gas). This was done because of the low spectral resolutions of the G430L and G750L gratings, which made it challenging to separate different kinematic components in cases where lines are heavily blended. Nonetheless, in order to improve the accuracy of the fits to the weaker emission lines and blends in the spectra, we used the kinematics (velocity shifts and widths) derived from fits to the [O III] doublet in each aperture to constrain the fits to the other key diagnostic lines used in our analysis, such as Hβ, Hγ, [O III] λ4363, [O II] λλ3726,3729, [O II] λλ7319,7331, [S II] λλ4068,4076, [S II] λλ6717,6731, [Ar IV] λλ4711,4740, and He II λ4686. We found that this procedure produced acceptable fits to these lines, including the TR [S II] λλ4068,4076 and [O II] λλ7319,7331 doublets. However, for closely spaced doublets such as [O II] λ3726,3729, the low spectral resolution meant that we did not resolve individual lines, and so we modelled the *total* doublet profile as a single emission line during the fitting process.

4 ANALYSIS OF THE STIS SPECTRA

4.1 Transauroral line diagnostics

In order to provide estimates of the electron densities of the warm ionized gas in NGC 1068 and NGC 4151, we make use of a technique first described by Holt et al. (2011), which requires measurement of the TR [S II] and [O II] ratios:

$$TR([O\,II]) = F(3726 + 3729)/F(7319 + 7331),$$
$$TR([S\,II]) = F(4068 + 4076)/F(6717 + 6731).$$

In this technique, measured TR([O II]) and TR([S II]) ratios are compared to those expected from photoionization modelling in order to simultaneously derive electron densities and reddenings. This has several important advantages as a density diagnostic over commonly used, traditional methods. First, these lines have higher critical densities (Appendix A), meaning that the TR ratios are sensitive to higher electron densities ($n_e \sim 10^{5.5}$ cm^{-3}) than the traditional [O II](3726/3729) and [S II](6717/6731) density diagnostics, which are only sensitive up to $n_e \sim 10^{3.5}$ cm^{-3}. Furthermore, the TR method uses the ratios of the *total* line fluxes of widely separated emission-line doublets, unlike the traditional [S II] and [O II] techniques, which rely on the flux ratios of lines *within* the doublets. This means that the TR ratios are less susceptible to uncertainties from fit degeneracy resulting from the larger velocity widths (as often seen for outflowing gas) and low spectral resolutions (as for our STIS spectra) that lead to blending of line profiles within the doublets.

We used the [O III] model fits to the TR lines to measure line fluxes, which were then used to calculate measured TR ratios. The CLOUDY code (version C17.02: Ferland et al. 2017) was then used to generate plane-parallel, single-slab, radiation-bounded models of solar-composition gas with no dust depletion, photoionized by a central source. We set the ionizing continuum of this source to follow a power-law of shape $F_v \propto v^{-\alpha}$ between 10 μm and 50 keV, with a spectral index of $\alpha = 1.5$. This is close to the average optical to X-ray spectral index measured in radio-quiet AGN (Zamorani et al. 1981; Miller et al. 2011) and is consistent with photoionization modelling of the emission-line ratios of the extended and nuclear NLRs in various samples of AGN (e.g. Ferland & Netzer 1983, Robinson et al. 1987). We note, however, that the TR ratios are relatively insensitive to the shape of the ionizing continuum (see Appendix B of Santoro et al. 2020). We selected an ionization parameter of log $U = -3$ (the highest value that reproduced the measured TR ratios) and varied the electron density of the modelled gas in 0.01 dex steps between $2.00 < \log_{10}(n_e \text{ [cm}^{-3}]) < 5.00$. We then reddened the modelled TR
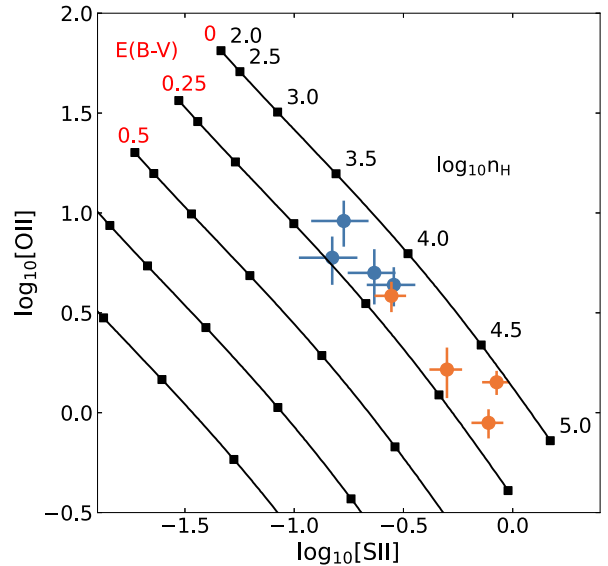

Figure 4. Grid of modelled TR (TR) [S II] and [O II] line ratios for radiation-bounded gas at different electron densities and reddenings, (black joined squares; as modelled with the CLOUDY code and the CCM89 extinction curve) and measured line ratios for NGC 1068 (orange circles) and NGC 4151 (blue circles).

ratios generated for each electron density value with the $R_v = 3.1$ CCM89 law, producing a grid of values that we compared to our measured ratios in order to provide simultaneous values of electron density and reddening. The resulting TR grid is shown in Fig. 4, and the derived values are given in Table 1.

The electron densities measured in this way for NGC 1068 have values in the range $4.00 < \log_{10}(n_e \text{ [cm}^{-3}]) < 4.75$, while those for NGC 4151 are approximately an order of magnitude lower $(3.60 < \log_{10}(n_e \text{ [cm}^{-3}]) < 4.10)$. This is the first time that densities above $n_e = 10^{3.5}$ cm^{-3} have been found using the TR lines with *spatially resolved* observations, and agree with similarly high electron densities derived using this technique for non-spatially resolved observations of other AGN (e.g. Holt et al. 2011; Rose et al. 2018; Santoro et al. 2018; Spence et al. 2018; Davies et al. 2020; Speranza et al. 2022). Importantly, the densities we find here are above the critical densities of the traditional [O II](3726/3729) and [S II](6717/6731) line ratios (Appendix A), and since we do not separate broad (outflowing) and narrow (quiescent; non-outflowing) components, they are likely to be underestimates for the outflowing gas (which is expected to be denser than the quiescent gas: e.g. Villar-Martín et al. 1999; Holden et al. 2023). The reddenings that we measure are relatively modest and in the range $0.05 < E(B-V)_{TR} < 0.25$ for both objects – these values were used to deredden our spectra for all further analysis.

4.2 Ionization states and mechanisms of the warm gas

The relatively low-ionization TR lines must be emitted by radiation-bounded clouds. Therefore, it is uncertain how well densities derived from the TR ratios would represent the densities of clouds or cloud complexes that have been shock-ionized or have significant matter-bounded components. Furthermore, the model used in the TR ratio method assumes radiation-bounded AGN-photoionized clouds, with no contribution from a matter-bounded component or shock-ionization. Similarly, the multicomponent ionization modelling by Revalski et al. (2021) – which has previously been applied to

NGC 1068 and NGC 4151 – uses AGN photoionization models. Therefore, it is important to investigate the ionization mechanisms for the gas detected in our STIS slits, which potentially can also give information regarding the outflow acceleration mechanism(s) present.

4.2.1 Electron temperatures

Electron temperatures of the warm ionized phase are expected to be higher for shocked gas than AGN-photoionized gas (e.g. Fosbury et al. 1978; Villar-Martín et al. 1999). Therefore, to provide a first indication of the ionization mechanisms of the warm ionized gas observed in our apertures, we measured electron temperatures using the (dereddened) [O III](5007 + 4959)/4363 emission-line ratio and the PyNeb Python module (Luridiana, Morisset & Shaw 2015), taking the electron densities for the apertures to be those derived using the TR line technique for both objects ($3.75 < \log_{10}(n_e[\mathrm{cm}^{-3}]) < 4.75$: see Table 1 and Section 4.1). We present the measured electron temperatures in Table 1, which are found to be high ($14\,300 < T_e < 21\,000$ K) for every aperture in both objects, with particularly high temperatures (up to $T_e = 21\,000$ K) being found in the central apertures of NGC 4151. The high electron temperatures that we find in our apertures for both objects may not be fully explainable as being due to AGN-photoionization of radiation-bounded gas (Fosbury et al. 1978; Binette, Wilson & Storchi-Bergmann 1996; Villar-Martín et al. 1999; Holden et al. 2023).

4.2.2 Shock-ionization vs matter-bounded AGN photoionization

In order to investigate the cause of the high electron temperatures further, we produced the [O III](5007/4363) versus He II/Hβ diagnostic diagram developed by Villar-Martín et al. (1999), as shown in Fig. 5. The radiation-bounded photoionization models shown here are the same as those used for the TR ratio grid in Section 4.1 (Fig. 4), albeit for an electron density of $n_e = 10^4\,\mathrm{cm}^{-3}$, varying ionization parameters ($-3.5 < \log_{10} U < -2.0$), and two values of spectral index ($\alpha = 1.0, 1.5$). The pure shock and precursor (pre-shock) models are taken from the MAPPINGS III library presented by Allen et al. (2008), with varying shock velocities in the range $100 < v_{\mathrm{shock}} < 1000\,\mathrm{km\,s}^{-1}$ and magnetic parameters of $B/\sqrt{n} = 2,4\,\mu\mathrm{G\,cm}^{3/2}$ for a solar-composition pre-shock gas with a density of $n = 10^2\,\mathrm{cm}^{-3}$. The magnetic parameters were chosen to cover a reasonable range of values expected in the ISM (Dopita & Sutherland 1995), in addition to being close to the magnetic parameters near equipartition ($B/\sqrt{n} \sim 3.23\,\mu\mathrm{G\,cm}^{3/2}$: Allen et al. 2008). Note that we do not use the standard 'BPT' diagrams (Baldwin, Phillips & Terlevich 1981) to investigate the ionization of the gas, because some of the lines involved in those diagrams (such as Hα and [N II] $\lambda\lambda 6548,6583$) are strongly blended in our apertures due to the outflow kinematics and relatively low spectral resolution, and therefore are affected by major fit degeneracies.

In Fig. 5, we also plot [O III](5007/4363) and He II/Hβ as functions of $A_{\mathrm{M/I}}$: the ratio of the solid angles subtended by matter-bounded clouds and radiation-bounded clouds, from modelling by Binette et al. (1996). This ratio allows us to estimate the relative contribution of matter-bounded clouds and radiation-bounded clouds in our apertures. The modelling by Binette et al. (1996) assumes solar-metallicity gas, with an ionizing source spectral index of $\alpha = -1.3$, an ionization parameter of $\log U = -1.4$ and a density of $n_{\mathrm{MB}} = 50\,\mathrm{cm}^{-3}$. The radiation-bounded clouds are ionized by UV photons that have passed through the matter-bounded component, thus the shape of the ionizing spectrum reaching the radiation-bounded clouds
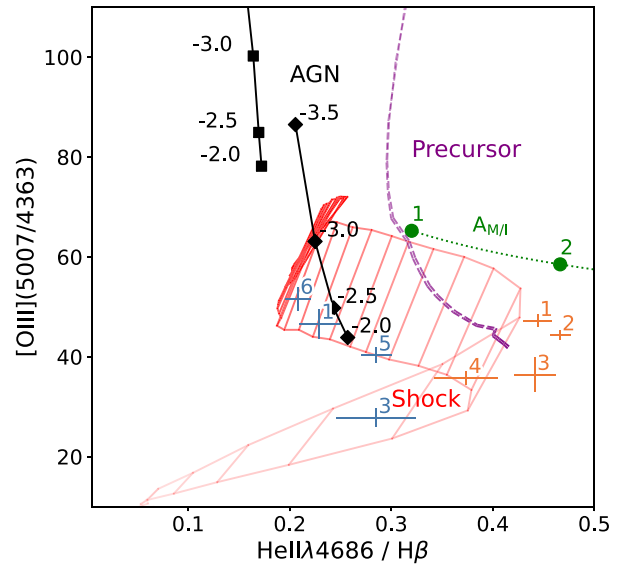

Figure 5. [O III](5007/4363) versus He II/Hβ diagnostic diagram (Villar-Martín et al. 1999), used to distinguish between radiation-bounded AGN-photoionization, matter-bounded AGN-photoionization and shock-ionization. The black markers show the predicted line ratios from radiation-bounded CLOUDY modelling (see Section 4.1) for solar-composition gas with a density of $n_e = 10^4\,\mathrm{cm}^{-3}$ and varying ionization parameters ($\log U$; labelled) and spectral indices (squares: $\alpha = 1.5$; diamonds: $\alpha = 1.0$). The solid red grid shows the line ratios predicted from shock modelling (Allen et al. 2008) for solar-composition gas with a pre-shock density of $n = 10^2\,\mathrm{cm}^{-3}$ and magnetic parameters of $B/\sqrt{n} = 2,4\,\mu\mathrm{G\,cm}^{3/2}$, with lighter regions on the plot corresponding to lower shock velocities. The purple dashed lines show the predicted emission from the precursor gas, which has not yet passed through (but is photoionized by) the shock, and the dotted green line shows the line ratios expected for different ratios of matter-bounded and radiation-bounded clouds ($A_{\mathrm{M/I}}$, labelled and marked with green circles) from modelling by Binette et al. (1996). Observed line ratios for each aperture are shown in orange for NGC 1068 and blue for NGC 4151, with the aperture number annotated.

has changed relative to that from the source – the parameters of the radiation-bounded clouds are determined using the resulting ionizing spectrum and by assuming that the clouds have fixed pressures.

Due to the continuum underlying the Hβ, [He II] $\lambda 4686$, and [O III] $\lambda 4363$ lines being more complex than that which underlies the [O III] $\lambda\lambda 4959,5007$ doublet and TR lines, we used a Markov Chain Monte Carlo (MCMC) fitting routine to fit the lines involved in the He II $\lambda 4686$/Hβ and [O III](5007/4363) ratios in each aperture for both objects – this was done to ensure that we were not significantly overestimating line flux uncertainties due to blending of spectral lines and the continuum. We used the results of the Gaussian fits described in Section 3.2.4 (determined using least squares optimization) to these lines as initial starting points for the MCMC routine, which fit the same models (namely one or two Gaussians and a low-order polynomial) to the spectra – taking into account the flux uncertainty of the HST data – with priors chosen to ensure the resulting models were physical (i.e. the line fluxes, mean wavelengths, and line widths must have been positive). For each fit, we initialized 500 walkers in a Gaussian distribution around the starting parameters and used a total of 5000 iterations (including a 1000 iteration 'burn-in' phase). The MCMC fits themselves were run using the EMCEE Python module (Foreman-Mackey et al. 2013).

From Fig. 5, we find clear evidence for significant matter-bounded emission in Apertures 1, 2, and 3 in NGC 1068, implied by high
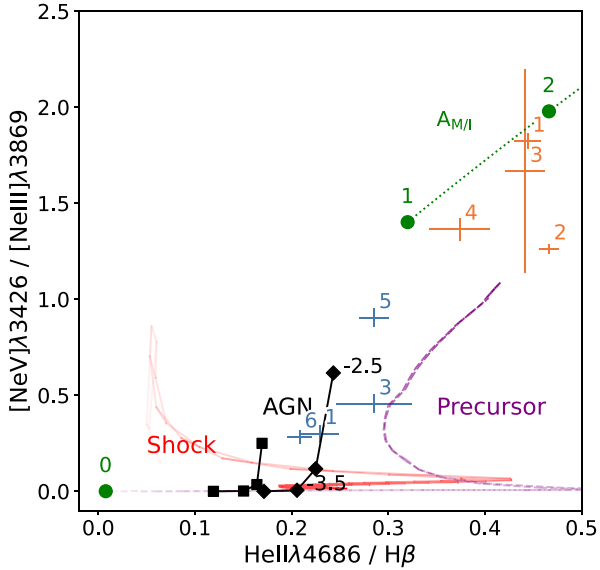
Figure 6. [Ne V]3426/[Ne III]3869 versus He II/Hβ diagnostic diagram – both ratios are sensitive to the presence of significant matter-bounded components. The line and marker scheme is the same as Fig. 5. The line ratios measured in our NGC 1068 apertures are located in the matter-bounded photoionization region of the diagram (corresponding to $1 < A_{M/I} < 2$; consistent with Fig. 6), whereas the NGC 4151 line ratios fall in the shock/precursor/radiation-bounded AGN photoionization region.

electron temperatures and He II/Hβ > 0.4 (similar ratio values were also measured by Kraemer & Crenshaw 2000b); the approximate ratio of matter-bounded to radiation-bounded clouds is $A_{M/I} \sim$ 2. The difference between the [O III](5007/4363) ratios measured in the NGC 1068 apertures and those predicted from the Binette et al. (1996) modelling can be explained as due to the models only representing one combination of parameters. It is possible for matter-bounded clouds with different parameters to have similar [O III](5007/4363) ratios to those found for NGC 1068. Specifically, this ratio would be smaller for higher electron densities than the low density assumed by Binette et al. (1996). Moreover, the presence of matter-bounded emission in these apertures is supported by the strength of high-ionization emission lines ($E_{ion} > 95$ eV), such as [Ne V] λ3426, [Fe VII] λ3759, and [Fe VII] λ6087, relative to lower-ionization lines (such as [O III]) in our STIS spectra. These and other high-ionization lines were previously identified in the same data set by Kraemer & Crenshaw (2000a). For Aperture 4 of NGC 1068 (centred slightly above the nucleus: Fig. 2), we measure He II/Hβ ratios consistent with both matter-bounded AGN-photoionization and shock-ionization.

To further probe the ionization mechanism of the gas, we also measured the [Ne V] λ3426/[Ne III] λ3869 ratio – which is sensitive to higher ionization gas – using the same MCMC fitting routine described earlier. We produced a diagnostic diagram of [Ne V] λ3426/[Ne III] λ3869 versus He II/Hβ using the same radiation-bounded photoionization, matter-bounded photoionization, and shock-ionization models as used for the [O III](5007/4363) and He II/Hβ diagram (Fig. 5), and present this in Fig. 6. We find that the values for all of the NGC 1068 apertures are consistent with matter-bounded AGN-photoionization with $1 < A_{M/I} < 2$. This further indicates that the gas in these apertures is matter-bounded and AGN-photoionized, including Aperture 4.

With the exception of Aperture 3, the [O III](5007/4363) versus He II/Hβ ratios measured in our NGC 4151 apertures (Fig. 5) are con-

sistent with both shock ionization and radiation-bounded AGN photoionization (assuming a relatively flat spectral index of $\alpha = 1.0$ and $\log U \sim -2.0$). However, from the [Ne V] λ3426/[Ne III] λ3869 versus He II/Hβ diagram (Fig. 6), it can be seen that the measured ratios for NGC 4151 are not consistent with pure shock-ionization alone: if the gas is shock ionized, then a contribution from the precursor component is required. Alternatively, the gas in these apertures may have pure radiation-bounded AGN photoionization; however, we highlight that this requires a relatively flat spectral index ($\alpha = 1.0$), and/or higher ionization parameters ($-3.0 < \log U < -2.0$) and densities ($n_e > 10^5$ cm^{-3}) than can explain our TR line ratios (Section 4.1). Ultimately, it is not possible to determine unambiguously the true, dominant ionization mechanism of the gas in our NGC 4151 apertures with the diagnostic features that are available in our data.

4.2.3 The viability of shock-ionization

In order to further investigate the viability of shocks as the dominant ionization mechanism along our slits for NGC 1068 and NGC 4151, we compared our measured Hβ fluxes to those expected from shock models – a technique presented by Baron et al. (2017). First, we converted our measured (and dereddened) Hβ fluxes ($F_{H\beta}$) into Hβ luminosities using the luminosity distances (D_L) for each galaxy. The resulting luminosities were then converted into luminosities per surface area using the aperture sizes in arcsec (i.e. the aperture width multiplied by the slit width) and the spatial scales for each object (0.067 kpc/arcsecond and 0.078 kpc/arcsecond, respectively).

We then compared the measured luminosities per surface area to those expected from the MAPPINGS III shock models of pre-shock density $n = 10^2$ cm^{-3} (corresponding the densities measured in our apertures, assuming a compression factor of 100: Sutherland & Dopita 2017) and magnetic parameters $B/\sqrt{n} =$ 2, 4 µG cm$^{3/2}$. From this comparison, we find that the Hβ luminosities per surface area, as measured in each aperture for NGC 1068 ($4.9 \times 10^{-3} < L_{H\beta} < 2.2 \times 10^{-2}$ erg s^{-1} cm^{-2}) and NGC 4151 ($2.2 \times 10^{-3} < L_{H\beta} < 4.6 \times 10^{-3}$ erg s^{-1} cm^{-2}), can be accounted for by shocks with velocities $v_{shock} > 425$ km s^{-1} and $v_{shock} > 225$ km s^{-1} respectively. In both cases, the outflow velocities for our apertures (Section 4.4.1; Table 2) are above these required velocities. This demonstrates that shock-ionization *could* feasibly produce the recombination line fluxes measured in both objects; however, this alone does not necessarily confirm the ionization mechanism.

Note that here we assumed a gas covering factor of unity relative to the shock (i.e. that the emitting-gas covers the entire area of the shock within each aperture), this may not be the case in reality. If this covering factor is in fact much lower than unity, then a larger shock area or higher shock velocities would be needed to produce the same Hβ luminosity.

4.3 The high-ionization gas in NGC 1068

The relative strengths of the high ionization ($E_{ion} > 95$ eV) lines detected in several of our apertures for NGC 1068 indicate the presence of matter-bounded clouds, which may play an important role in the structure of the cloud complexes present in the NLR. Determining the physical conditions of this high-ionization component is therefore necessary. To this end, we measured the [Fe VII](6087/3759) and [Ne V] λ3426/[Fe VII] λ6086 emission-line ratios, which are sensitive to the density and ionization parameter of the high-ionization gas. These ratios were calculated using the measured line fluxes of the lines in the ratios, which were themselves determined using the same MCMC fitting method described in Section 4.2.

Table 2. Outflow velocities, outflow masses, mass outflow rates, kinetic powers and coupling efficiencies for the apertures of our STIS spectra of NGC 1068 and NGC 4151. The outflow velocities used to calculate the mass outflow rates and kinetic powers presented here are from the CKN1068 and CKN4151 models (see Section 4.4.1).

| Aperture	v_{out} (km s^{-1})	M_{out} (M$_\odot$)	$\dot{M}_{out}$ (M$_\odot$yr^{-1})	$\dot{E}_{kin}$ (W)	ϵ_f (per cent)
			NGC 1068		
1	-1300	$(1.7 \pm 0.3) \times 10^5$	3.7 ± 0.6	$(2.0 \pm 0.3) \times 10^{35}$	$(4.9 \pm 0.7) \times 10^{-1}$
2	-1100	$(6.3 \pm 0.8) \times 10^4$	1.6 ± 0.2	$(6.1 \pm 0.7) \times 10^{34}$	$(1.5 \pm 0.2) \times 10^{-1}$
3	-450	$(7.3 \pm 0.9) \times 10^4$	1.2 ± 0.1	$(7.6 \pm 0.9) \times 10^{33}$	$(1.9 \pm 0.2) \times 10^{-2}$
4	-150	$(9.4 \pm 2.2) \times 10^4$	$(6.0 \pm 1.4) \times 10^{-1}$	$(4.2 \pm 1.0) \times 10^{32}$	$(1.1 \pm 0.2) \times 10^{-3}$
			NGC 4151		
1	-700	$(2.5 \pm 0.6) \times 10^5$	3.7 ± 1.0	$(5.8 \pm 0.2) \times 10^{34}$	$(4.1 \pm 1.1) \times 10^{-1}$
3	-800	$(7.2 \pm 3.0) \times 10^4$	3.4 ± 1.4	$(6.9 \pm 2.9) \times 10^{34}$	$(4.9 \pm 2.0) \times 10^{-1}$
5	800	$(1.7 \pm 0.4) \times 10^5$	4.5 ± 1.2	$(9.2 \pm 2.4) \times 10^{34}$	$(6.5 \pm 1.7) \times 10^{-1}$
6	800	$(2.9 \pm 0.7) \times 10^5$	6.9 ± 1.8	$(1.4 \pm 0.4) \times 10^{35}$	$(9.9 \pm 2.6) \times 10^{-1}$
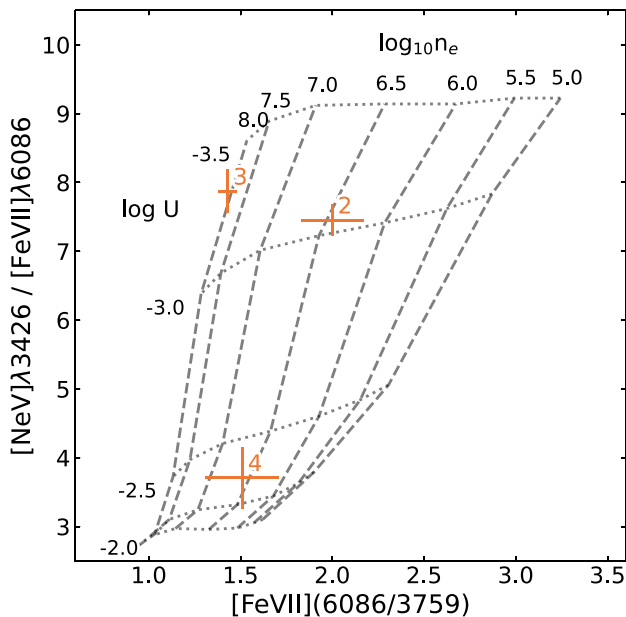
Figure 7. [Fe VII](6087/3759) vērsus [Ne V] λ3426/[Fe VII] λ6086 diagnostic diagram, sensitive to the spectral index, ionization parameter, and electron density of the gas. The grey grid was generated using CLOUDY for radiation-bounded AGN-photoionization with a spectral index of $\alpha = 1.5$ (see Appendix B) and varying electron densities and ionization parameters: dashed lines connect points of constant density (labelled), and dotted lines connect points of constant ionization parameter (also labelled). The measured ratio values in our NGC 1068 apertures are shown in orange and labelled. From this diagram, the high ionization gas is found to have densities in the range $6.45 < \log_{10}(n_e[\text{cm}^{-3}]) < 8.00$.

We present the [Fe VII](6087/3759) versus [Ne V] λ3426/[Fe VII] λ6086 diagnostic diagram (see Rose et al. 2011) with our measured line ratios for the NGC 1068 apertures in Fig. 7; a CLOUDY radiation-bounded photoionization grid for a solar metallicity, plane-parallel, single-slab cloud of varying ionization parameters ($-3.5 < \log U < -2.0$) and electron densities ($5.0 < \log (n_e[\text{cm}^{-3}]) < 8.0$), and a central ionizing source with spectral index $\alpha = 1.5$ (see Appendix B), is shown. From this grid, we determine the densities of the high-ionization gas to be in the range $6.45 < \log_{10}(n_e[\text{cm}^{-3}]) < 8.00$: several orders of magnitude higher than the gas traced by the lower critical-density [O II] and

[S II] lines. We discuss the implications of this for the gas structures within our apertures in Section 5.2.1.

4.4 Energetics of the outflowing gas

4.4.1 Outflow kinematics

In order to determine the mass outflow rates, kinetic powers, and coupling efficiencies of the gas outflows detected in our STIS spectra, we required measurements of the kinematics of the outflowing gas.[3] For this purpose, we used the results from detailed kinematic modelling (based the same HST/STIS spectra used here) of NGC 1068 and NGC 4151 presented by Crenshaw & Kraemer (2000b) and Crenshaw et al. (2000; hereafter CKN1068 and CKN4151), respectively. We note that, due to the different PAs used and the fact that the outflow geometry likely depends greatly on PA, we do not use the updated kinematic models from Das et al. (2005) and Das et al. (2006).

To calculate deprojected velocities, we first derived a universal 'deprojection factor' by dividing the maximum observed velocities (located at the velocity 'turnover' position – see Crenshaw & Kraemer 2000b and Crenshaw et al. 2000) by the maximum model-deprojected velocities from the CKN1068 and CKN4151 bicone models. We then took the the highest observed (projected) velocity at the position of each aperture, and divided these velocities by our determined deprojection factor to give the maximum deprojected outflow velocity in each aperture. We label the deprojected outflow velocities as v_{out}, and give their values in Table 2.

4.4.2 Mass outflow rates, kinetic powers, and coupling efficiencies

We used the Hβ luminosities to determine masses for the warm ionized gas in each aperture with

$$M_{ion} = \frac{L(H\beta)m_p}{\alpha_{H\beta}^{eff} h v_{H\beta} n_e}, \tag{1}$$

where M_{ion} is the total mass of the warm ionized gas, m_p is the proton mass, $\alpha_{H\beta}^{eff}$ is the Case B recombination coefficient for Hβ (taken to be 1.61×10^{-14} cm^{3}s^{-1} for a gas of density $n_e = 10^4$ cm^{-3} and temperature $T_e = 20\,000$ K; Osterbrock & Ferland 2006), and $v_{H\beta}$ is the frequency of the Hβ line.

---

[3]We do not use kinematics derived from our [O III] models due to the relatively low spectral resolution and high instrumental widths of our spectra.

Assuming that the derived masses (estimated using the total line fluxes) are dominated by outflowing gas, we combined them with the aperture crossing time to calculate mass outflow rates

$$\dot{M}_{\text{out}} = \frac{M_{\text{ion}} v_{\text{out}}}{\Delta R}, \tag{2}$$

where v_{out} is the outflow velocity from the CKN1068 and CKN4151 models, and ΔR is the aperture width.

Kinetic powers were estimated from the mass outflow rates using

$$\dot{E}_{\text{kin}} = \frac{1}{2} \dot{M}_{\text{out}} v_{\text{out}}^2. \tag{3}$$

Finally, the ratio of the kinetic power to the bolometric AGN luminosity (L_{bol}) was taken to estimate coupling efficiencies for each aperture:

$$\epsilon_{\text{f}} = \frac{\dot{E}_{\text{kin}}}{L_{\text{bol}}}. \tag{4}$$

NGC 1068 is estimated to have a bolometric luminosity in the range $0.4 < L_{\text{bol}} < 4.7 \times 10^{38}$ W (Woo & Urry 2002; Alonso-Herrero et al. 2011; Lopez-Rodriguez et al. 2018; Gravity Collaboration 2020), of which we take the lowest value to ensure higher estimates of coupling efficiencies and thus determine the maximum potential impact of the outflowing gas on the host galaxy. For NGC 4151, we took the bolometric luminosity to be $L_{\text{bol}} = 1.4 \times 10^{37}$ W (Kraemer et al. 2020).

We present our derived mass outflow rates, kinetic powers, and coupling efficiencies for both cases in Table 2. For NGC 1068, our estimates are less than the maximum values determined from photoionization modelling by Revalski et al. (2021; $\dot{M}_{\text{out}} = 9.0 \pm 1.13\,\text{M}_\odot\,\text{yr}^{-1}$; $\dot{E}_{\text{kin}} = (5.4 \pm 0.5) \times 10^{35}$ W, $\epsilon_{\text{f}} = 0.54 \pm 0.05$ per cent).[4] For NGC 4151, our derived values are similar to the results of photoionization modelling by Crenshaw et al. (2015; $\dot{M}_{\text{out}} \sim 3.01 \pm 0.45\,\text{M}_\odot\,\text{yr}^{-1}$; $\dot{E}_{\text{kin}} = (4.3 \pm 1.0) \times 10^{34}$ W, $\epsilon_{\text{f}} = 0.54 \pm 0.11$ per cent). Our calculated mass outflow rates for NGC 4151 are also consistent with previous values derived for the warm ionized phase by Storchi-Bergmann et al. (2010; $M_{\text{out}} \approx 2.4\,\text{M}_\odot$) and the X-ray emitting gas ($M_{\text{out}} \approx 2\,\text{M}_\odot\,\text{yr}^{-1}$: Wang et al. 2011b and Kraemer et al. 2020).

For NGC 1068, the mass outflow rates for the warm-ionized phase are much below that of the cold molecular gas at a similar extent from the nucleus (i.e. traced by CO, HCN; $T \sim 100$ K): García-Burillo et al. (2014) derive a mass outflow rate of $\dot{M}_{\text{out}} = 63^{+21}_{-37}\,\text{M}_\odot\,\text{yr}^{-1}$ within the $r \sim 200$ pc circumnuclear disc of NGC 1068. This indicates that most of the outflowing mass may be present in the colder gas phases, as has been found for other objects (see Ramos Almeida et al. 2019 and Holden et al. 2023).

5 DISCUSSION

From our analysis of archival STIS spectra of the central regions ($r < 160$ pc) of NGC 1068 and NGC 4151, we find evidence for dense ($10^{3.6}\,\text{cm}^{-3} < n_e < 10^{4.8}\,\text{cm}^{-3}$) gas that shows line ratios consistent with matter-bounded AGN-photoionization in the case of NGC 1068, and shock-ionization (with precursor gas ionization) or radiation-bounded AGN-photoionization in the case of NGC 4151. Furthermore, we find that the measured Hβ luminosities could be explained as being due to shock-ionization for both objects, assuming

---

[4]Crenshaw et al. (2015) and Revalski et al. (2021) assume bolometric luminosities of Lbol = 1×10^{38} W for NGC 1068 and Lbol = 7.9×10^{36} W for NGC 4151 when calculating coupling efficiencies.

a shock covering factor of unity. In both objects, we find coupling efficiencies that are close to the lowest value required by models of galaxy evolution. In this section, we discuss the implication of these results on the dominant ionization and acceleration mechanisms of the gas seen in our slits, compare our results to past work on these two well-studied objects, and investigate the impact on the density diagnostic techniques used. Finally, we place our results in a broader context by comparing with those from a similar study of the nearby Seyfert 2 galaxy IC 5063.

5.1 The outflow ionization and acceleration mechanisms in the NLRs of NGC 1068 and NGC 4151

To determine the true impact of the outflowing gas on the host galaxies, quantitative comparison of observations to theoretical modelling is needed. However, both modelling of jet–ISM interactions (e.g. Mukherjee et al. 2018; Audibert et al. 2023) and AGN radiation-pressure-driven outflows (e.g. Crenshaw & Kraemer 2000b; Meena et al. 2023) are able to explain outflow kinematics in different objects. In order to enable accurate future comparisons to theoretical models and therefore accurately quantify the impact of the outflows in NGC 1068 and NGC 4151 – which have been conversely argued to be radiatively accelerated (Crenshaw et al. 2000; Crenshaw & Kraemer 2000b; Das et al. 2005, 2006; Revalski et al. 2021; Meena et al. 2023) and jet-accelerated (Capetti et al. 1997; Axon et al. 1998; May & Steiner 2017; May et al. 2020) – the dominant outflow acceleration mechanisms in these objects need to be robustly identified.

5.1.1 Matter-bounded ionization and the acceleration mechanism in NGC 1068

It has been previously proposed that the outflows in NGC 1068 are driven via radiation pressure (Kraemer & Crenshaw 2000a; Das et al. 2006; Revalski et al. 2021; Meena et al. 2023) instead of shocks induced by the radio jet colliding with the ISM within the bicone. While we do not separate the outflowing gas from the quiescent gas in this work, our results are consistent with this mechanism: we find evidence for matter-bounded AGN-photoionization of the warm-ionized gas in the form of simultaneous high [O III] temperatures (Table 1: $T_e \sim 15\,000$ K; corresponding to [O III](5007/4363) < 60) and line ratios (He II $\lambda 4686$ / Hβ > 0.4: Fig. 5; [Ne V] $\lambda 3426$ / [Ne III] $\lambda 3869$ > 1.0: Fig. 6) within a 134 pc radius from the nucleus in the NE cone along the radio axis, consistent with radiative acceleration. However, it is *possible* that the outflowing gas has been shock-ionized and accelerated by the jet but has subsequently cooled and then been reionized by the AGN (e.g. Holden et al. 2023). Spatially resolved, high spectral-resolution observations are needed to further investigate this situation by separating the emission from the outflowing and quiescent gas, and then determining the ionization and excitation mechanisms of each kinematic component. In addition, comparing the electron densities of the outflowing and non-outflowing gas may reveal signs of shock compression, which is expected to be a factor of $\sim$4–100 (Sutherland & Dopita 2017).

We note that the outflowing gas appears to be spatially confined to the extent of the radio structure: the broad (FWHM$_v$ > 250 km s^{-1}) [O III] $\lambda\lambda 4959,5007$ emission in our spectra is seen to a maximum radius of $\sim$4.8 arcsec from the nucleus in the NE cone (as measured from the line profiles of the [O III] emission that extends beyond the regions covered by our apertures), similar to the maximum radial extent of the NE radio lobe (6.18 arcsec; 420 pc) measured from radio imaging (e.g. 15 GHz: Wilson & Ulvestad 1987 5 GHz:

Wilson & Ulvestad 1983, Gallimore et al. 1996; 22 GHz: Gallimore et al. 1996; 1.4 GHz: Gallimore et al. 1996, García-Burillo et al. 2014). This is also in agreement with ground-based Fabry–Pérot integral field spectroscopy by Cecil et al. (1990) – which finds no significant velocity deviation from the systematic velocity beyond the radio lobe – and kinematic modelling by Crenshaw & Kraemer (2000b), Das et al. (2006), and Meena et al. (2023), which find outflows extended up to ∼5.1 arcsec from the nucleus.[5] Furthermore, VLT/MUSE spectroscopy presented by Venturi et al. (2021) shows that the measured [O III] W70 velocity parameter[6] has high values (400 km s^{-1} < [O III] W70 < 1200 km s^{-1}) between the nucleus and the lobe, out to a radius of 3.6 arcsec along the bicone axis. Moreover, the NLR molecular CO(3–2) outflows (as seen in ALMA imaging by García-Burillo et al. 2014) decelerate within the radio lobe, at a distance of ∼400 pc (∼5.7 arcsec) from the nucleus. Taken together, this shows that the NE cone outflows have a similar extent to the NE radio lobe. This is evidence for the outflows being accelerated by the radio jet, although it does not entirely rule out radiative acceleration.

5.1.2 Shock-ionization and acceleration in NGC 4151

Our results for NGC 4151 indicate that the near-nuclear gas along the radio axis may be shock-ionized since the measured [O III](5007/4363), He II/Hβ, and [Ne V] λ3426/[Ne III] λ3869 line ratios and Hβ luminosities are consistent with those expected from a mixture of shock and shock-precursor ionization (Figs 5 and 6; Section 4.2.3).

The radio structure in the NLR of NGC 4151, as seen in low-resolution 1.5–5 GHz VLA radio imaging by Johnston et al. (1982), has a lobe-like component with a centroid 6.43 arcsec from the nucleus along the radio axis in the NE cone. This structure lies beyond the maximum ∼4 arcsec extent of the warm-ionized outflows (Meena et al. 2023; see also Das et al. 2005), and – as we have argued for the situation in NGC 1068 – is consistent with the outflows being launched by the radio jet. From HST/PC + HST/WFPC2 imaging, Williams et al. (2017) found higher [O III]/Hα ratios close to the string of radio knots that are seen in their higher-resolution 1.51 GHz observations (shown here in Fig. 1), with the values of this ratio decreasing beyond ∼4 arcsec from the nucleus along the radio axis. The authors interpreted this as the radio jet having a contribution to the ionization of the gas close to the nucleus, but AGN-photoionization being dominant further out. This is also in agreement with the results from X-ray and optical imaging by Wang et al. (2011a), who propose a mixture of shock-ionization and AGN-photoionization in the NLR of NGC 4151.

Taken together with the findings of these previous investigations, the results presented here may indicate that the outflows in NGC 4151 have been shock-accelerated and then re-ionized by photons from the AGN, with AGN-photoionization being dominant further from the nucleus.

---

[5] An [O III] emission knot in the NLR of NGC 1068, labelled 'A' by Meena et al. (2023) and located 7.3 arcseconds from the nucleus (i.e. beyond the radio source), has outflow-like kinematics (200 < FWHM < 1000 kms^{-3}; v_{out} = 863 kms^{-3}). As noted by Meena et al. (2023), this knot lies beyond the expected extent of radiatively driven outflows. Regardless, we highlight that the vast majority of the outflows along the radio axis are located at lower radii than the maximum extent of the NE radio lobe.

[6] W70 is defined as the difference between the velocities that contain 85 per cent and 15 per cent of the total flux of the fits to the line profile (see Venturi et al. 2021).

5.2 The effect of ionization mechanisms on density diagnostics

The ionization mechanisms (Section 4.2), electron temperatures (Section 4.2.1), and densities (Sections 4.1 and 4.3) of the warm gas detected in our STIS slits allow us to investigate the structures and conditions of the line-emitting clouds, and therefore verify the origin of different emission lines and thus the precision of diagnostics that make use of them. For example, the TR density diagnostic (Section 4.1) relies on AGN-photoionization being dominant, with no significant contribution from a matter-bounded component or shock-ionization. Since we find evidence for matter-bounded emission in NGC 1068 and potential shock-ionization in NGC 4151, it is important to investigate the effect of this on derived densities.

5.2.1 The impact of matter-bounded photoionization

If the higher ionization lines are indeed emitted by matter-bounded gas structures in the outflow (as shown by the [O III] temperatures, He II/Hβ ratios, and [Fe VII](6086/3759) versus [Ne V] λ3426/[Fe VII] λ6086 diagram: Sections 4.2 and 4.3), then the TR lines cannot be emitted by the same structures. However, it is possible that they are emitted by different clouds within the same cloud complexes, considering that we see these lines with similar profiles in each of our apertures. Alternatively, or perhaps in addition, it is possible that the outer layers of a single cloud are matter-bounded, while the denser core is radiation-bounded (one of the scenarios presented by Binette et al. 1996). In this scenario, the matter-bounded layers may represent lower density gas that was driven away from the ionization front by the increase in pressure that occurred when the gas structure was first photoionized by the AGN. However, this is not consistent with our findings; in Section 4.3, we use the [Fe VII](6087/3759) and [Ne V] λ3426/[Fe VII] λ6086 emission-line ratios to determine high-ionization gas densities of 6.45 < log$_{10}$(n_e[cm^{-3}]) < 8.00 in our NGC 1068 apertures: significantly higher than that of the lower-ionization gas. A potential explanation is that the gas that is emitting the high-ionization [Fe VII] and [Ne V] lines represents dense fragments of the expanding matter-bounded component: since these lines have high critical densities (7.1 < log$_{10}$(n_{crit}[cm^{-3}]) < 8.5; Appendix A), they would only be emitted strongly by such dense cloud components.

Therefore, given the ionization energies of the lines (Appendix A), we propose that the [Fe VII] and [Ne V] lines trace matter-bounded, higher ionization clouds within the complexes (or edges of individual clouds), and the [O II] and [S II] lines are emitted from radiation-bounded clouds (or cores of individual clouds). In this scenario, much of the [O III] emission must arise from the matter-bounded regime in order to explain the high electron temperatures that we measure in our NGC 1068 apertures (Section 4.2.1). Hence, given the high density of the high-ionization gas, it is likely that the gas emitting the [O III] lines is denser than the gas that is emitting the TR lines. This reinforces the need for outflow diagnostics that are sensitive to high (>10$^{3.5}$ cm^{-3}) densities.

5.2.2 The impact of shock-ionization

Since the gas in our NGC 4151 apertures may be shock-ionized, it is essential to quantify the effect of this on the TR ratio density diagnostic. In Appendix C, we plot the TR ratios from shock models over the TR photoionization diagnostic grid used in Section 4.1 and quantify the impact of shock-ionization on the TR electron density and reddening values derived from the photoionization grid. We find that, overall, the effect on the derived density is ±0.38

orders of magnitude, and the effect on derived reddenings is E(B-V)±0.13. Crucially, we note that this is much less than the impact of using lower-critical-density techniques (such as the [S II](6717/6731) ratio) and is similar to the effect of varying the parameters of the photoionization model (Santoro et al. 2020: $\log(n_e[\mathrm{cm}^{-3}])$ ±(0.1–0.7); E(B-V)±(0.1–0.2)). In summary, while using the TR line method presented by Holt et al. (2011) as a density and reddening diagnostic for shock-ionized gas does incur some uncertainty on the derived densities, the derived densities are still likely more accurate than those derived from commonly used, traditional methods.

Gas that has been shock-ionized by jet–ISM interactions presents a problem for the photoionization modelling method used by Revalski et al. (2021), as the technique relies on assuming that the material at a given distance from the nucleus is being photoionized by the central AGN engine. In the case of shock-ionization, the outflows are instead being shock-ionized *locally* by the jet within the bicone at any given distance from the nucleus, and so any electron densities derived using an assumed ionization parameter and distance will be incorrect. Revalski et al. (2021) used the standard BPT diagrams (Baldwin et al. 1981) in an attempt to ensure all of the measured line ratios were consistent with AGN-photoionization. However, the regions of AGN shock and photoionization in these diagrams overlap considerably, thus further diagnostics should also be used in order to disentangle the contribution from shocks and photoionization, such as the [O III](5007/4363) versus He II λ4686/Hβ (Villar-Martín et al. 1999) and [Fe II] λ12570/Paβ versus H_2λ21218/Brγ (Rodríguez-Ardila, Riffel & Pastoriza 2005; Riffel et al. 2013; Colina et al. 2015; Riffel et al. 2021; Holden et al. 2023) diagnostic diagrams, and/or the 3D diagram (which makes use of line ratios and velocity dispersion) presented by D'Agostino et al. (2019).

Overall, despite the challenges that shock-ionization and significant matter-bounded photoionization components present to the TR line technique and the Revalski et al. (2021) photoionization modelling, we argue that these methods are nonetheless more robust density diagnostics than the commonly used [S II](6717/6731) and [O II](3726/3729) ratios. In the case of matter-bounded photoionization, the [S II] λλ6717,6731 and [O II] λλ3726,3729 lines arise from the same part of the ionization structure of the cloud as the TR lines, meaning they face the same issues as the TR method, while the Revalski et al. (2021) modelling allows for higher-ionization components, and therefore is a more accurate diagnostic of the overall cloud density. Furthermore, we have established here that using radiation-bounded photoionization grids to measure the TR densities of shock-ionized gas incurs an uncertainty on the overall density that is much less than using lower-critical density line ratios for high-density ($n_e > 10^3 \mathrm{cm}^{-3}$) gas: in the case of NGC 4151 (where there may be some contribution from shock-ionization), the TR-derived densities are similar to those reported by Revalski et al. (2022; see also Crenshaw et al. 2015), indicating that both methods still give more precise density determinations than traditional methods, despite some of their underlying assumptions potentially being incorrect.

5.3 Comparison of the TR electron densities to other techniques

Using the TR method, we find high electron densities in both objects: $4.00 < \log(n_e[\mathrm{cm}^{-3}]) < 4.75$ in NGC 1068 and $3.50 < \log(n_e[\mathrm{cm}^{-3}]) < 4.10$ in NGC 4151 (Section 4.1; Table 1). This agrees with the similarly high densities ($> 10^3 \mathrm{cm}^{-3}$) derived from multicomponent photoionization modelling of both objects presented in Crenshaw et al. (2015) and Revalski et al. (2021; see also Collins et al. (2009) and Revalski et al. 2022). Crucially, the derived densities from both techniques lie above the sensitivity

range of the traditional [S II](6717/6731) and [O II](3726/2739) techniques, which are commonly used (either directly or as a basis for assumption) to derive electron densities in studies of the warm-ionized phase (e.g. Nesvadba et al. 2006; Liu et al. 2013; Harrison et al. 2014; Fiore et al. 2017), thus further supporting the need for robust warm-ionized gas electron density diagnostics such as the TR line technique and multicomponent photoionization modelling.

Considering the traditional [S II](6717/6731) ratio, Kraemer & Crenshaw (2000a; using the same STIS data set as used in this work) and Kakkad et al. (2018) and Mingozzi et al. (2019; using IFU data) derived electron densities of $n_e \sim 10^3 \mathrm{cm}^{-3}$ for the outflows in the NLR of NGC 1068. These [S II]-derived densities are 1–1.5 orders of magnitude lower than those we find using the TR method, and are close to the upper limit of the density range for the [S II] ratio technique (Appendix A: $n_{\mathrm{crit}} \sim 10^{3.5} \mathrm{cm}^{-3}$). This provides further evidence that, for gas of electron density $n_e > 10^{3.5} \mathrm{cm}^{-3}$, the [S II](6717/6731) ratio may underestimate the true electron density by more than an order of magnitude.

5.4 The impact of the outflowing gas on the host galaxies

Using densities derived from the TR line ratios, reddening-corrected recombination line fluxes and kinematics taken from previous modelling, we find mass outflow rates in the range $0.6 < \dot{M}_{\mathrm{out}} < 6.9 \mathrm{M}_\odot \mathrm{yr}^{-1}$, and coupling efficiencies in the range $1.1 \times 10^{-3} < \epsilon_{\mathrm{kin}} < 0.99$ per cent (Table 2). In many cases, our calculated coupling efficiencies are just above the lower limit required by models of the co-evolution of galaxies and their supermassive black holes (e.g. ∼0.5–10 per cent; Di Matteo et al. 2005; Springel et al. 2005; Hopkins & Elvis 2010). It is important to note that there is likely more outflowing material within the bicones that is not covered by our slits (which are only 0.1 arcsec wide), and that comparisons between coupling efficiencies from models and observations are not straightforward (see Harrison et al. 2018 for further discussion). To properly account for the impact of the warm ionized outflows, detailed studies that make use of robust density diagnostics, separate emission from the outflowing and quiescent gas and, importantly, cover the entire NLRs of both objects, are needed. Moreover, we highlight that assessments of *all* gas phases – not just the warm ionized phase – are needed to robustly assess the *total* impact of the AGN-driven outflows (Cicone et al. 2018), as the warm ionized gas may represent just a fraction of the total outflowing gas mass at a given radius (e.g. Ramos Almeida et al. 2019; Holden et al. 2023). Therefore, it is likely the the true coupling efficiencies of the total NLR outflows in NGC 1068 and NGC 4151 are higher than we calculate here.

5.5 A tale of three Seyferts: NGC 1068, NGC 4151 and IC 5063

Finally, using the results for the nearby Seyfert 2 IC 5063 presented in Holden et al. (2023), along with the results for NGC 1068 and NGC 4151 that we present here, we can begin to construct a sample of nearby Seyferts with spatially resolved, detailed studies of their NLR outflows.

IC 5063 is a nearby ($z = 0.01131$) early type Seyfert 2 galaxy that is seen close to edge-on, with a radio jet propagating almost in the plane of the disc that drives fast ($v_{\mathrm{out}} > 700 \mathrm{km\,s}^{-1}$) outflows (Morganti, Oosterloo & Tsvetanov 1998; Oosterloo et al. 2000; Morganti et al. 2015; Mukherjee et al. 2018; Holden et al. 2023). These outflows are seen in multiple gas phases, including warm ionized (Morganti et al. 2007; Sharp & Bland-Hawthorn 2010; Congiu et al. 2017; Venturi et al. 2021; Holden et al. 2023); neutral (Morganti et al. 1998; Oosterloo et al. 2000); warm molecular (Tadhunter et al. 2014;
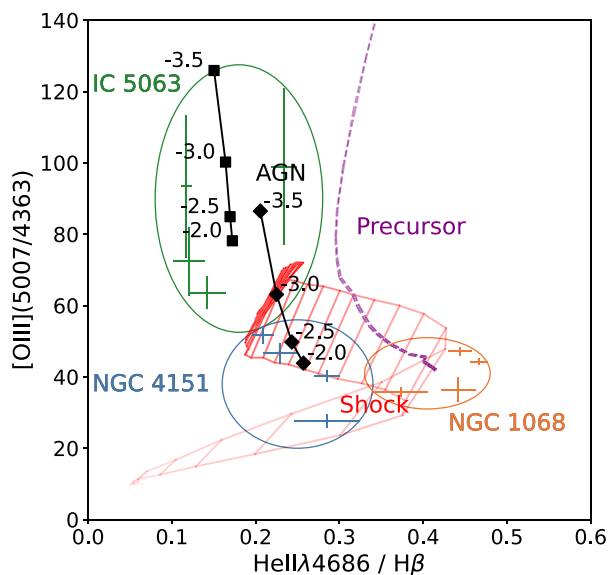
Figure 8. [O III](5007/4363) versus He II4686/Hβ diagnostic diagram (as in Fig. 5) with line ratios measured from the STIS spectra of NGC 1068 and NGC 4151 (presented in this work) and from Xshooter spectra of IC 5063 (presented in Holden et al. 2023). The AGN, shock, and precursor models are the same as those described in Section 4.2. The three objects each show distinct ionization conditions, hinting at the complex nature of the NLRs of Seyfert galaxies.

Holden et al. 2023) and cold molecular (Morganti et al. 2013, 2015; Dasyra et al. 2016; Oosterloo et al. 2017).

In Holden et al. (2023), we presented evidence that both the outflowing and quiescent warm ionized gas in IC 5063 has dominant AGN-photoionization – even though the outflows show clear signatures of shock acceleration – and that the different outflow phases may represent a post-shock cooling sequence. We interpreted this situation as the pre-shock gas being AGN-photoionized, and the closest post-shock gas to the AGN kept in an ionized state by photoionization. In Fig. 8, we add the [O III](5007/4363) and He II4686/Hβ ratios for IC 5063 from Holden et al. (2023) to the diagnostic diagram presented in this work (Fig. 5). Furthermore, we present [O II](7319 + 7331)/[O III] λ5007 and [S II](4068 + 4076)/Hβ ratios for IC 5063 (alongside NGC 1068 and NGC 4151) in Appendix D (Fig. D1) – determined using the data set from Holden et al. (2023) – and find that they are consistent with radiation-bounded AGN-photoionization with gas densities 10^3 cm$^{-3} < n_e < 10^4$ cm^{-3} and ionization parameters in the range $-3 < \log U < -2$, in agreement with the values determined in Holden et al. (2023).

It is interesting that the overall differences in ionization conditions *between* the three galaxies are significantly larger than the range of ionization conditions *within* the galaxies. Our small sample thus shows three distinct cases in the three objects: radiation-bounded AGN-photoionization in IC 5063, matter-bounded AGN-

photoionization in NGC 1068, and shock-ionization or radiation-bounded AGN photoionization with a relatively flat spectral index and higher ionization parameters in NGC 4151 – despite all being classified as Seyferts, the details of the ionization mechanisms in the objects vary greatly. This is particularly interesting considering that in all three objects, the outflows detected along the radio axes appear to be spatially confined to the radio structures (i.e. the outflows do not extend beyond the radio lobes in the NLRs). As argued in Section 5.1, this is consistent with shock-acceleration, although it does not rule out radiative-acceleration. If the outflows in IC 5063, NGC 1068 and NGC 4151 are shock-accelerated, then this would highlight the importance of not deriving information regarding the outflow acceleration mechanisms based solely on the ionization/excitation mechanisms or kinematics of the gas in NLRs: a full account, involving detailed multiwavelength observations with multiple diagnostics, is required to properly evaluate the relative contributions of different mechanisms.

Despite evidence that the outflows in all three objects are being driven by the radio jet, the densities of the outflowing gas differ by more than an order of magnitude. For IC 5063, we found that the outflowing gas has densities in the range $3.17 < \log(n_e[\text{cm}^{-3}]) < 3.43$, while for NGC 1068 and NGC 4151, we find densities in the ranges $4.00 < \log(n_e[\text{cm}^{-3}]) < 4.75$ and $3.50 < \log(n_e[\text{cm}^{-3}]) < 4.10$, respectively (Table 1). The reason for this may simply be due to different pre-shock gas densities in the different objects (assuming the outflows in all three are shock-accelerated). For IC 5063, the pre-shock density is $2.1 < \log(n_e[\text{cm}^{-3}]) < 2.7$; however, without higher velocity resolution spectra, we are unable to determine the quiescent gas densities in NGC 1068 and NGC 4151. In addition, the differing post-shock densities in the three Seyferts may be due to different cooling conditions behind the shock front. Standard shock-jump conditions predict a compression factor of $\sim$4; however, this may be much higher ($\sim$100) if the post-shock gas has cooled in pressure equilibrium (Sutherland & Dopita 2017; Santoro et al. 2018).

Moreover, all three objects have low-to-intermediate radio luminosities ($1.6 \times 10^{22} < L_{1.4\,\text{GHz}} < 3.0 \times 10^{23}$ W Hz^{-1}; Table 3) – again, if the outflows in these Seyferts are shock-accelerated, then this would reinforce the importance of jet-driven shocks as a feedback mechanism in the inner regions of galaxies, even at lower radio luminosities, in agreement with a statistical study of nearby AGN presented by Mullaney et al. (2013). Furthermore, the radio jets in NGC 1068 and NGC 4151 are oriented out of galactic discs by $\sim$45° and $\sim$36°, respectively, unlike IC 5063, in which the jet propagates almost directly into the plane of the disc. Therefore, at least within the central few hundred parsecs of the AGN, this would show that inclined jets can still have an impact on the kinematics and ionization of the NLR, as predicted by recent relativistic hydrodynamic simulations (Mukherjee et al. 2018; Meenakshi et al. 2022), which show that a jet inclined $\theta_{\text{jet}} \sim 45°$ to the galaxy's disc may have a significant effect on the kinematics, density, and temperature of the gas within the central few kpc (albeit less so than a jet inclined in the plane of the disc, such as is the case

Table 3. Bolometric luminosities, 1.4 GHz radio luminosities, jet powers (P$_{\text{jet}}$), jet orientations with respect to the disc (θ_{jet}) and ionization mechanisms detected along the radio axis for NGC 1068, NGC 4151, and IC 5063.

Object	L_{bol} (W)	$L_{1.4\,\text{GHz}}$ (W Hz^{-1})	P$_{\text{jet}}$ (W)	θ_{jet}	Ionization mechanism[a]
NGC 1068	0.4–4.7×10^{38}	2.3×10^{23}	1.8×10^{36} (García-Burillo et al. 2014)	$\sim$45°	Matter-bounded photoionization
NGC 4151	1.4×10^{37}	1.6×10^{22}	$\sim 10^{35}$ (Wang et al. 2011b)	$\sim$36°	Photo- and/or shock-ionization
IC 5063	7.6×10^{37}	3×10^{23}	10^{37-38} (Mukherjee et al. 2018)	$\sim$5°	Radiation-bounded photoionization

[a]Determined with line ratios detected in slits along PA = 202° (NGC 1068), PA = 70° (NGC 4151), and PA = 115° (IC 5063).

in IC 5063). Similar hydrodynamic simulations, specifically tailored to the situations in NGC 1068 and NGC 4151, could thus be used to quantify the impact of their radio jets on the star-forming gas in their NLRs, as well as the impact of inclined kpc-scale jets in general.

Ultimately, further observations of NGC 1068 and NGC 4151 are required to decisively determine the outflow acceleration mechanism(s). Namely, wide wavelength coverage spectroscopy (to make available a range of diagnostics) with sufficient velocity resolution to kinematically discriminate between outflowing (post-shock?) and quiescent (pre-shock?) gas.

6 CONCLUSIONS

By analysing archival HST/STIS spectra taken along the radio axes of the inner few hundred parsecs of the NLR of the prototypical Seyfert galaxies NGC 1068 and NGC 4151, we have found the following.

(i) Using the TR line ratio technique, we derive spatially resolved electron densities of $4.00 < \log_{10} n_e [\mathrm{cm}^{-3}]) < 4.75$ for NGC 1068 and $3.60 < \log_{10} n_e [\mathrm{cm}^{-3}]) < 4.10$ for NGC 4151. These values are an order of magnitude above those commonly reported and assumed based on traditional density estimates, but are in agreement with the results from alternative diagnostics such as multicomponent photoionization modelling. Overall, our results provide further motivation for the use of the TR lines in deriving electron densities of AGN-driven outflows.

(ii) The measured emission-line ratios for the warm ionized gas are consistent with the dominant ionization mechanisms being matter-bounded AGN-photoionization in NGC 1068 and shock-ionization and/or radiation-bounded AGN-photoionization with a relatively flat spectral index (and/or higher ionization parameters and lower metallicities) in NGC 4151.

(iii) Along the radio axes, the outflows in the north-eastern cones of both objects have similar spatial extents to the radio structures – this is consistent with the outflows in their NLRs being shock-accelerated by the radio jets and reionized by radiation from the AGN, although it does not rule out radiative acceleration.

(iv) Applying the TR line technique to gas that has dominant shock-ionization may incur an uncertainty on the derived electron densities by up to ± 0.38 orders of magnitude, which is still far below the potential order-of-magnitude error incurred when using techniques that are not sensitive to higher density gas. However, care must still be taken when using detailed density diagnostic techniques, as the ionization mechanism of the gas may alter the results. Therefore, robust ionization-mechanism diagnostics should be used to verify the validity of the density measurements.

(v) Finally, by combining our findings with those for the nearby Seyfert 2 galaxy IC 5063, we find that the ionization mechanisms and outflow conditions along the radio axes in the central few hundred parsecs vary significantly between the different objects. Thus, overall, our study highlights the necessity of care when deriving information about outflow acceleration mechanisms from the ionization of the gas, and the need for robust ionization-mechanism diagnostics with detailed observations.

ACKNOWLEDGEMENTS

DATA AVAILABILITY

The data used in this report are available from the HLA (https://hla.stsci.edu/hlaview.html) with proposal IDs GTO:5754 (PI Ford) and GTO:5124 (PI Ford) for the HST/WFPC2 [O III] imaging, and proposal IDs GTO:7573 (PI Kraemer) and GTO:7569 (PI Hutchings) for the HST/STIS spectra.

REFERENCES

Allen M. G., Groves B. A., Dopita M. A., Sutherland R. S., Kewley L. J., 2008, ApJS, 178, 20
Alonso-Herrero A. et al., 2011, ApJ, 736, 82
Antonucci R. R. J., Miller J. S., 1985, ApJ, 297, 621
Astropy Collaboration, 2013, A&A, 558, A33
Astropy Collaboration, 2018, ApJ, 156, 123
Audibert A. et al., 2023, A&A, 671, L12
Axon D. J., Marconi A., Capetti A., Macchetto F. D., Schreier E., Robinson A., 1998, ApJ, 496, L75
Baldwin J. A., Phillips M. M., Terlevich R., 1981, PASP, 93, 5
Barbosa F. K. B., Storchi-Bergmann T., McGregor P., Vale T. B., Rogemar Riffel A., 2014, MNRAS, 445, 2353
Baron D., Netzer H., 2019, MNRAS, 486, 4290
Baron D., Netzer H., Poznanski D., Prochaska J. X., Förster Schreiber N. M., 2017, MNRAS, 470, 1687
Binette L., Wilson A. S., Storchi-Bergmann T., 1996, A&A, 312, 365
Boyce J. C., Menzel D. H., Payne C. H., 1933, Proc. Natl. Acad. Sci., 19, 581
Capetti A., Macchetto F. D., Lattanzi M. G., 1997, ApJ, 476, L67
Cardelli J. A., Clayton G. C., Mathis J. S., 1989, ApJ, 345, 245 (CCM89)
Carral P., Turner J. L., Ho P. T. P., 1990, ApJ, 362, 434
Cecil G., Bland J., Tully R. B., 1990, ApJ, 355, 70
Cicone C. et al., 2014, A&A, 562, A21
Cicone C., Brusa M., Ramos Almeida C., Cresci G., Husemann B., Mainieri V., 2018, Nat. Astron., 2, 176
Colina L. et al., 2015, A&A, 578, A48
Collins N. R., Kraemer S. B., Crenshaw D. M., Bruhweiler F. C., Meléndez M., 2009, ApJ, 694, 765
Congiu E. et al., 2017, MNRAS, 471, 562
Crenshaw D. M., Kraemer S. B., 2000a, ApJ, 532, 247
Crenshaw D. M., Kraemer S. B., 2000b, ApJ, 532, L101 (CKN1068)
Crenshaw D. M. et al., 2000, AJ, 120, 1731 (CKN4151)
Crenshaw D. M., Fischer T. C., Kraemer S. B., Schmitt H. R., 2015, ApJ, 799, 83
Currie M. J., Berry D. S., Jenness T., Gibb A. G., Bell G. S., Draper P. W., 2014, in Manset N., Forshay P., eds, ASP Conf. Ser. Vol. 485, Astronomical Data Analysis Software and Systems XXIII. Astron. Soc. Pac., San Francisco, p. 391
D'Agostino J. J., Kewley L. J., Groves B. A., Medling A., Dopita M. A., Thomas A. D., 2019, MNRAS, 485, L38
Das V. et al., 2005, AJ, 130, 945
Das V., Crenshaw D. M., Kraemer S. B., Deo R. P., 2006, AJ, 132, 620
Dasyra K. M., Combes F., Oosterloo T., Oonk J. B. R., Morganti R., Salomé P., Vlahakis N., 2016, A&A, 595, L7
Davé R., Anglés-Alcázar D., Narayanan D., Li Q., Rafieferantsoa M. H., Appleby S., 2019, MNRAS, 486, 2827

Davies R. et al., 2020, MNRAS, 498, 4150
Di Matteo T., Springel V., Hernquist L., 2005, Nature, 433, 604
Dopita M. A., Sutherland R. S., 1995, ApJ, 455, 468
Dubois Y., Peirani S., Pichon C., Devriendt J., Gavazzi R., Welker C., Volonteri M., 2016, MNRAS, 463, 3948
Evans I. N., Ford H. C., Kinney A. L., Antonucci R. R. J., Armus L., Caganoff S., 1991, ApJ, 369, L27
Fabian A. C., 1999, MNRAS, 308, L39
Ferland G. J., Netzer H., 1983, ApJ, 264, 105
Ferland G. J. et al., 2017, Rev. Mex. Astron. Astrofis., 53, 385
Ferrarese L., Merritt D., 2000, ApJ, 539, L9
Fiore F. et al., 2017, A&A, 601, A143
Fischer T. C. et al., 2017, ApJ, 834, 30
Foreman-Mackey D., Hogg D. W., Lang D., Goodman J., 2013, PASP, 125, 306
Fosbury R. A. E., Mebold U., Goss W. M., Dopita M. A., 1978, MNRAS, 183, 549
Gallimore J. F., Baum S. A., O'Dea C. P., Pedlar A., 1996, ApJ, 458, 136
García-Burillo S. et al., 2014, A&A, 567, A125
García-Burillo S. et al., 2019, A&A, 632, A61
Gebhardt K. et al., 2000, ApJ, 539, L13
González Delgado R. M., Leitherer C., Heckman T. M., 1999, ApJS, 125, 489
Gravity Collaboration, 2020, A&A, 634, A1
Harris C. R. et al., 2020, Nat., 585, 357
Harrison C. M., Alexander D. M., Mullaney J. R., Swinbank A. M., 2014, MNRAS, 441, 3306
Harrison C. M., Costa T., Tadhunter C. N., Flütsch A., Kakkad D., Perna M., Vietri G., 2018, Nature Astron, 2, 198
Holden L. R., Tadhunter C. N., Morganti R., Oosterloo T., 2023, MNRAS, 520, 1848
Holt J., Tadhunter C. N., Morganti R., Emonts B. H. C., 2011, MNRAS, 410, 1527
Hopkins P. F., Elvis M., 2010, MNRAS, 401, 7
Hutchings J. B. et al., 1999, AJ, 118, 2101
Johnston K. J., Elvis M., Kjer D., Shen B. S. P., 1982, ApJ, 262, 61
Kakkad D. et al., 2018, A&A, 618, A6
Kraemer S. B., Crenshaw D. M., 2000a, ApJ, 532, 256
Kraemer S. B., Crenshaw D. M., 2000b, ApJ, 544, 763
Kraemer S. B., Turner T. J., Couto J. D., Crenshaw D. M., Schmitt H. R., Revalski M., Fischer T. C., 2020, MNRAS, 493, 3893
Liu G., Zakamska N. L., Greene J. E., Nesvadba N. P. H., Liu X., 2013, MNRAS, 436, 2576
Lopez-Rodriguez E. et al., 2018, ApJ, 859, 99
Luridiana V., Morisset C., Shaw R. A., 2015, A&A, 573, A42
Magorrian J. et al., 1998, ApJ, 115, 2285
Mandal A., Mukherjee D., Federrath C., Nesvadba N. P. H., Bicknell G. V., Wagner A. Y., Meenakshi M., 2021, MNRAS, 508, 4738
May D., Steiner J. E., 2017, MNRAS, 469, 994
May D., Steiner J. E., Menezes R. B., Williams D. R. A., Wang J., 2020, MNRAS, 496, 1488
Meena B., Crenshaw D. M., Schmitt H. R., Revalski M., Fischer T. C., Polack G. E., Kraemer S. B., Dashtamirova D., 2021, ApJ, 916, 31
Meena B. et al., 2023, ApJ, 943, 98
Meenakshi M., Mukherjee D., Wagner A. Y., Nesvadba N. P. H., Morganti R., Janssen R. M. J., Bicknell G. V., 2022, MNRAS, 511, 1622
Miller B. P., Brandt W. N., Schneider D. P., Gibson R. R., Steffen A. T., Wu J., 2011, ApJ, 726, 20
Mingozzi M. et al., 2019, A&A, 622, A146
Morganti R., Oosterloo T., Tsvetanov Z., 1998, ApJ, 115, 915
Morganti R., Holt J., Saripalli L., Oosterloo T. A., Tadhunter C. N., 2007, A&A, 476, 735
Morganti R., Frieswijk W., Oonk R. J. B., Oosterloo T., Tadhunter C., 2013, A&A, 552, L4
Morganti R., Oosterloo T., Oonk J. B. R., Frieswijk W., Tadhunter C., 2015, A&A, 580, A1
Mukherjee D., Wagner A. Y., Bicknell G. V., Morganti R., Oosterloo T., Nesvadba N., Sutherland R. S., 2018, MNRAS, 476, 80
Mullaney J. R., Alexander D. M., Fine S., Goulding A. D., Harrison C. M., Hickox R. C., 2013, MNRAS, 433, 622
Müller Sánchez F., Davies R. I., Genzel R., Tacconi L. J., Eisenhauer F., Hicks E. K. S., Friedrich S., Sternberg A., 2009, ApJ, 691, 749
Mundell C. G., Wrobel J. M., Pedlar A., Gallimore J. F., 2003, ApJ, 583, 192
Nelson C. H., Weistrop D., Hutchings J. B., Crenshaw D. M., Gull T. R., Kaiser M. E., Kraemer S. B., Lindler D., 2000, ApJ, 531, 257
Nesvadba N. P. H., Lehnert M. D., Eisenhauer F., Gilbert A., Tecza M., Abuter R., 2006, ApJ, 650, 693
Oosterloo T. A., Morganti R., Tzioumis A., Reynolds J., King E., McCulloch P., Tsvetanov Z., 2000, ApJ, 119, 2085
Oosterloo T., Raymond Oonk J. B., Morganti R., Combes F., Dasyra K., Salomé P., Vlahakis N., Tadhunter C., 2017, A&A, 608, A38
Osterbrock D. E., Ferland G. J., 2006, Astrophysics of Gaseous Nebulae and Active Galactic Nuclei. University Science Books, Sausalito, CA
Osterbrock D. E., Koski A. T., 1976, MNRAS, 176, 61P
Pedlar A., Howley P., Axon D. J., Unger S. W., 1992, MNRAS, 259, 369
Pedlar A., Kukula M. J., Longley D. P. T., Muxlow T. W. B., Axon D. J., Baum S., O'Dea C., Unger S. W., 1993, MNRAS, 263, 471
Raban D., Jaffe W., Röttgering H., Meisenheimer K., Tristram K. R. W., 2009, MNRAS, 394, 1325
Ramos Almeida C., Acosta-Pulido J. A., Tadhunter C. N., González-Fernández C., Cicone C., Fernández-Torreiro M., 2019, MNRAS, 487, L18
Revalski M., Crenshaw D. M., Kraemer S. B., Fischer T. C., Schmitt H. R., Machuca C., 2018, ApJ, 856, 46
Revalski M. et al., 2021, ApJ, 910, 139
Revalski M. et al., 2022, ApJ, 930, 14
Riffel R. A., 2021, MNRAS, 506, 2950
Riffel R., Rodríguez-Ardila A., Aleman I., Brotherton M. S., Pastoriza M. G., Bonatto C., Dors O. L., 2013, MNRAS, 430, 2002
Riffel R. A., Vale T. B., Storchi-Bergmann T., McGregor P. J., 2014, MNRAS, 442, 656
Riffel R. A., Bianchin M., Riffel R., Storchi-Bergmann T., Schönell A. J., Dahmer-Hahn L. G., Dametto N. Z., Diniz M. R., 2021, MNRAS, 503, 5161
Robinson A., Binette L., Fosbury R. A. E., Tadhunter C. N., 1987, MNRAS, 227, 97
Robinson A. et al., 1994, A&A, 291, 351
Rodríguez-Ardila A., Riffel R., Pastoriza M. G., 2005, MNRAS, 364, 1041
Rose M., Tadhunter C. N., Holt J., Ramos Almeida C., Littlefair S. P., 2011, MNRAS, 414, 3360
Rose M., Tadhunter C., Ramos Almeida C., Rodríguez Zaurín J., Santoro F., Spence R., 2018, MNRAS, 474, 128
Santoro F., Rose M., Morganti R., Tadhunter C., Oosterloo T. A., Holt J., 2018, A&A, 617, A139
Santoro F., Tadhunter C., Baron D., Morganti R., Holt J., 2020, A&A, 644, A54
Schaye J. et al., 2015, MNRAS, 446, 521
Schlafly E. F., Finkbeiner D. P., 2011, ApJ, 737, 103
Schlegel D. J., Finkbeiner D. P., Davis M., 1998, ApJ, 500, 525
Seyfert C. K., 1943, ApJ, 97, 28
Sharp R. G., Bland-Hawthorn J., 2010, ApJ, 711, 818
Silk J., Rees M. J., 1998, A&A, 331, L1
Somerville R. S., Hopkins P. F., Cox T. J., Robertson B. E., Hernquist L., 2008, MNRAS, 391, 481
Spence R. A. W., 2018, PhD thesis, University of Sheffield, available at: https://etheses.whiterose.ac.uk/23431/
Spence R. A. W., Tadhunter C. N., Rose M., Rodríguez Zaurín J., 2018, MNRAS, 478, 2438
Speranza G. et al., 2022, A&A, 665, A55
Springel V., Di Matteo T., Hernquist L., 2005, MNRAS, 361, 776
Storchi-Bergmann T., McGregor P. J., Riffel R. A., Simões Lopes R., Beck T., Dopita M., 2009, MNRAS, 394, 1148
Storchi-Bergmann T., Lopes R. D. S., McGregor P. J., Riffel R. A., Beck T., Martini P., 2010, MNRAS, 402, 819
Sun A.-L., Greene J. E., Zakamska N. L., 2017, ApJ, 835, 222
Sutherland R. S., Dopita M. A., 2017, ApJS, 229, 34

Tadhunter C., 2016, A&AR, 24, 10

Tadhunter C., Morganti R., Rose M., Oonk J. B. R., Oosterloo T., 2014, Nat., 511, 440

Ulvestad J. S., Wilson A. S., 1984, ApJ, 285, 439

Venturi G. et al., 2021, A&A, 648, A17

Villar-Martín M., Tadhunter C., Morganti R., Axon D., Koekemoer A., 1999, MNRAS, 307, 24

Wagner A. Y., Bicknell G. V., 2011, ApJ, 728, 29

Wang J., Fabbiano G., Elvis M., Risaliti G., Mundell C. G., Karovska M., Zezas A., 2011a, ApJ, 736, 62

Wang J. et al., 2011b, ApJ, 742, 23

Williams D. R. A. et al., 2017, MNRAS, 472, 3842

Wilson A. S., Ulvestad J. S., 1983, ApJ, 275, 8

Wilson A. S., Ulvestad J. S., 1987, ApJ, 319, 105

Winge C., Axon D. J., Macchetto F. D., Capetti A., 1997, ApJ, 487, L121

Woo J.-H., Urry C. M., 2002, ApJ, 579, 530

Yuan W. et al., 2020, ApJ, 902, 26

Zamorani G. et al., 1981, ApJ, 245, 357

APPENDIX A: CRITICAL DENSITIES AND IONIZATION ENERGIES FOR THE EMISSION LINES USED IN OUR ANALYSIS

In Table A1, we present critical densities and ionization energies for the lines used in our analysis, calculated using the PYNEB PYTHON module for a gas of temperature $T_e = 15\,000$ K.

Previously, there have been concerns that the TR lines – used to derive electron densities and reddenings in Section 4.1 – do not trace the same gas that is emitting other key diagnostic lines such as Hβ and [O III] $\lambda\lambda$4959,5007 (see Sun, Greene & Zakamska 2017, Rose et al. 2018, Spence et al. 2018 and Holden et al. 2023). We note that, if the TR lines originate from denser clumps of gas within the same cloud complexes as the clouds emitting other lines (Sun et al. 2017), we would also expect those clumps to also radiate strongly in Hβ since the recombination line emissivity scales as n^2. Furthermore, we note that the TR lines have critical densities that are closer to the

Table A1. Critical densities and ionization energies at $T_e = 15\,000$ K for several key diagnostic lines that trace the warm ionized outflow phase: the [Ne V] λ3426 and [Ne III] λ3869 lines are used to investigate the presence of matter-bounded gas (Section 4.2); the lines in the [Fe VII](6087/3759) ratio are used to determine densities for high ionization gas (Section 4.3); the [O III] λ4959,5007 doublet is used for kinematics (Section 4.4.1); the [S II](6717/6731) and [S II](3726/3729) are 'traditional' density ratios, and the TR lines are used in the TR method to derive electron densities and reddenings (Section 4.1). The PYNEB PYTHON module was used to produce the values in this table.

Emission line	n_{crit} (cm^{-3})	E_{ion} (eV)
[Fe VII] λ6087	1.9×10^7	125.0
[Fe VII] λ3759	3.5×10^8	125.0
[Ne V] λ3426	1.8×10^7	126.2
[Ne III] λ3869	1.3×10^7	63.4
[O III] λ4959,5007	7.8×10^5	54.9
TR [O II] and [S II] lines		
[O II] λ7320,7331	6.9×10^6	35.1
[O II] λ7319,7330	4.7×10^6	35.1
[S II] λ4069	3.2×10^6	23.3
[S II] λ4076	1.6×10^6	23.3
Traditional [O II] and [S II] lines		
[O II] λ3726	4.8×10^3	35.1
[O II] λ3729	1.4×10^3	35.1
[S II] λ6716	1.9×10^3	23.3
[S II] λ6731	5.1×10^3	23.3

critical density of the [O III] $\lambda\lambda$4959,5007 lines than the traditional [S II] and [O II] lines (Table A1), so they are more likely to trace the [O III]-emitting clouds than the traditional lines (Rose et al. 2018; Spence et al. 2018). Furthermore, the TR ratios involve emission lines that arise from transitions within the [O II] ion, which has an ionization energy that is closer to the ionization energy of [O III] than [S II]. This highlights that the TR lines are likely better tracers of the [O III]-emitting gas than the commonly used [S II](6717/6731) ratio.

APPENDIX B: VARIATION OF THE [FE VII](6086/3759) VERSUS [NE V] λ3426/[FE VII] λ6086 DIAGNOSTIC DIAGRAM WITH SPECTRAL INDEX

The ratios used in the [Fe VII](6086/3759) versus [Ne V] λ3426/[Fe VII] λ6086 diagnostic diagram (Section 4.3; Fig. 7) are sensitive to both electron density and temperature, and thus the position of the AGN-photoionization grid on this diagram – which we use to determine the density of the high ionization gas – changes with the assumed ionizing source spectral index (α) and ionization parameter (U) of the gas. To further investigate this beyond only varying the ionization parameter (as is shown in Fig. 7 for $\alpha = 1.5$), here we show the effect of assuming a lower spectral index. We used the same CLOUDY model as described in Section 4.3, but instead took the spectral index to be $\alpha = 1.0$. We present the resulting grid (along with the grid for $\alpha = 1.5$ for comparison purposes) in Fig. B1.

From Fig. B1, it can be seen that a flatter spectral index produces lower [Ne V] λ3426/[Fe VII] λ6086 ratios, with little effect on the [Fe VII](6086/3759) ratios: for low values of [Ne V] λ3426/[Fe VII] λ6086 (i.e. as measured in Aperture 4 for NGC 1068), the effect on derived density is small ($\sim$0.1 dex).
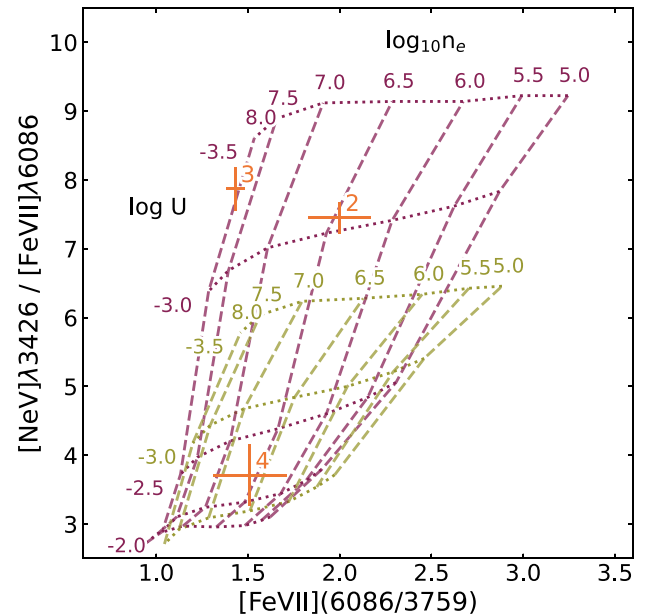

Figure B1. [Fe VII](6087/3759) versus [Ne V] λ3426/[Fe VII] λ6086 diagnostic diagram, as in Fig. 7, with radiation-bounded AGN-photoionization grids generated with CLOUDY for two values of spectral index: $\alpha = 1.0$ (green) and $\alpha = 1.5$ (purple). Otherwise, the labelling, colour, marker, and line scheme is the same as in Fig. 7.

However, a shallower spectral index cannot reproduce higher values of [Ne V] $\lambda 3426$/[Fe VII] $\lambda 6086$ (as measured in NGC 1068 apertures 2 and 3) without very low (log $U < -3.0$) ionization parameters. Therefore, we use the CLOUDY grid with $\alpha = 1.5$ to derive electron densities for the high ionization gas in Section 4.3.

APPENDIX C: MODELLING THE EFFECT OF SHOCK-IONIZATION ON THE TRANSAURORAL LINE RATIO DENSITY DIAGNOSTIC GRID

In order to investigate the effect of shock-ionization on the TR technique,[7] in Fig. C1, we plot the expected TR([O II]) and TR([S II]) line ratios with the radiation-bounded diagnostic grid for photoionized gas that we previously presented in Section 4.1 (Fig. 4). The shock models shown on this grid were taken from the library presented by Allen et al. (2008; generated with the MAPPINGS III code) and are for solar-composition gas.
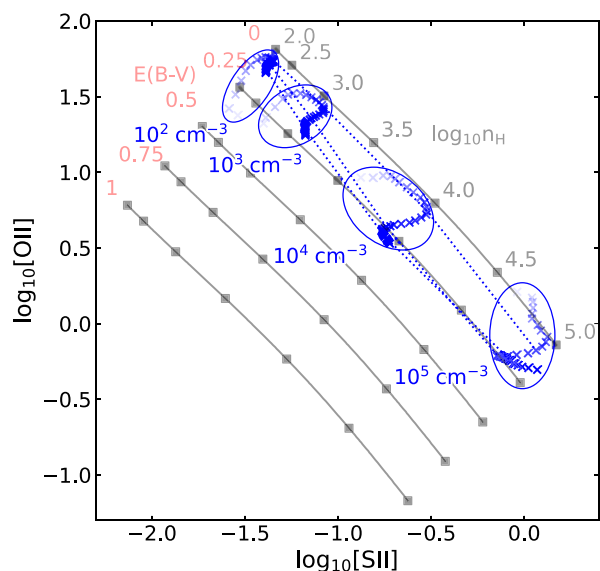

Figure C1. TR([S II]) versus TR([O II]) grid for radiation-bounded AGN-photoionized gas [black with red E(B-V) labels; as in Fig. 4] with the line ratios expected from modelled shocks (blue crosses) of fixed magnetic parameter ($B/\sqrt{n} = 2\,\mu\mathrm{G}\,\mathrm{cm}^{3/2}$) at different post-shock densities (labelled in blue) and for a range of shock velocities ($0 < v_{\mathrm{shock}} < 1000\,\mathrm{km\,s}^{-1}$). Line ratios from shock modelling at a single post-shock density (assuming a compression factor of 100) are grouped by blue ellipses, and points of the same shock velocity ($v_{\mathrm{shock}} = 400$, 600, and $800\,\mathrm{km\,s}^{-1}$) are joined by dashed blue lines.

We first investigate the effect of varying the gas velocity between $0 < v_{\mathrm{shock}} < 1000\,\mathrm{km\,s}^{-1}$ with a constant magnetic parameter of $B/\sqrt{n} = 2\,\mu\mathrm{G}\,\mathrm{cm}^{3/2}$ and pre-shock densities of $n = 1$, 10, 100, and $1000\,\mathrm{cm}^{-3}$. Assuming a compression factor of ~ 100 if the gas cools in pressure equilibrium behind the shock (Sutherland & Dopita 2017; Santoro et al. 2018), these correspond to post-shock densities of $n = 10^2$, 10^3, 10^4, and $10^5\,\mathrm{cm}^{-3}$. From Fig. C1, it can be seen that for high shock velocities ($\gtrsim 500\,\mathrm{km\,s}^{-1}$) at a given density, the modelled line ratios are similar to those predicted by photoionization modelling. However, for lower shock velocities (a few hundred

---

[7]The effect of shock-ionization on TR line density and reddening diagnostic was investigated in a preliminary fashion by Spence (2018).
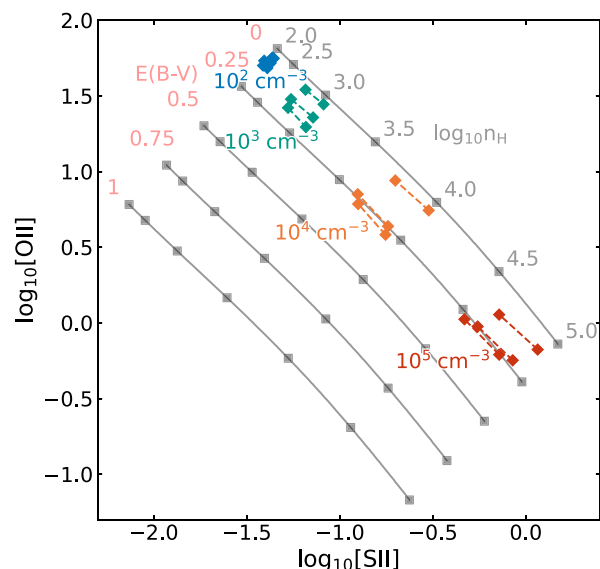

Figure C2. TR grid (as in Fig. 4) with line ratios predicted by shock modelling for three values of shock velocity $v_{\mathrm{shock}} = 400$, 600, and $800\,\mathrm{km\,s}^{-1}$ and two values of magnetic parameter ($2 < B/\sqrt{n} < 4\,\mu\mathrm{G}\,\mathrm{cm}^{3/2}$) that are typical of the ISM. Line ratios generated using the same post-shock density are shown as crosses with the same colour (labelled), and points of the same density and velocity are joined by a dashed line.
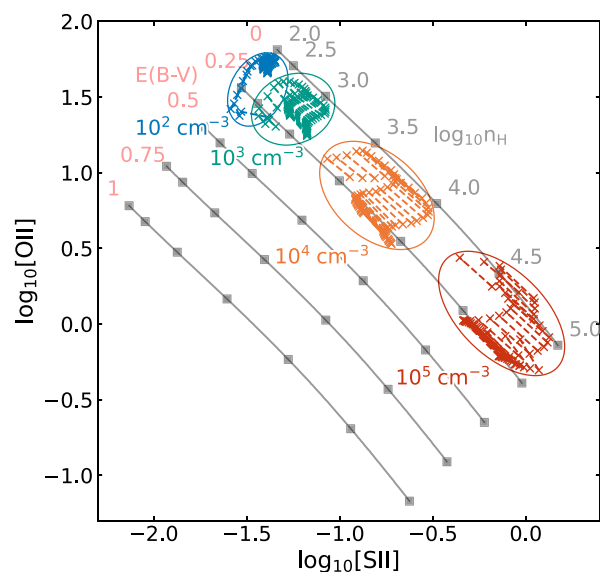

Figure C3. TR grid (as in Fig. 4) with line ratios predicted by shock modelling for two magnetic parameters ($B/\sqrt{n} = 2, 4\,\mu\mathrm{G}\,\mathrm{cm}^{3/2}$) and a range of shock velocities ($0 < v_{\mathrm{shock}} < 1000\,\mathrm{km\,s}^{-1}$) at each value of post-shock density. Predicted ratios with the same post-shock density are shown with crosses of a colour for each density (labelled) and are grouped with ellipses.

$\mathrm{km\,s}^{-1}$), the predicted densities may differ by ± 0.22 orders of magnitude. Similarly, shock-ionization may effect the derived colour excesses by E(B-V)$_{\mathrm{TR}} \pm 0.13$.

Secondly, we investigate the effect of varying the magnetic parameter between typical values for the ISM ($2 < B/\sqrt{n} < 4\,\mu\mathrm{G}\,\mathrm{cm}^{3/2}$: Dopita & Sutherland 1995; Allen et al. 2008). We did this for three values of shock velocity ($v_{\mathrm{shock}} = 400$, 600, and $800\,\mathrm{km\,s}^{-1}$), which we show in Fig. C2. The impact on derived electron densities is greater at higher densities (± 0.25 orders of magnitude) than at lower

densities (± 0.10 orders of magnitude), with little effect on the derived reddening value.

Finally, we quantify the effect of simultaneously varying the velocity (between $0 \, \mathrm{km \, s^{-1}} < v_{\mathrm{shock}} < 1000 \, \mathrm{km \, s^{-1}}$) and the magnetic parameter ($2 < B/\sqrt{n} < 4 \, \mu G \, \mathrm{cm^{3/2}}$) on the TR-derived electron densities and reddenings (Fig. C3). We find that the effect on the derived density is ± 0.38 orders of magnitude, regardless of the density of the modelled gas, and that the effect on derived reddening value is the same as varying the velocity (E(B-V)± 0.13).

APPENDIX D: THE ORIGIN OF THE TRANSAURORAL LINES IN NGC 1068, NGC 4151, AND IC 5063

In order to investigate the origin of the TR lines in the archetypal Seyfert galaxies (and the nearby Sey 2 IC 5063: Holden et al. 2023), we plotted the measured [O II](7319 + 7331)/[O III] $\lambda 5007$ versus [S II](4068 + 4076)/Hβ ratios with overlaid grids from radiation-bounded photoionization modelling (as first presented by Spence et al. 2018) and shock modelling, which we present in Figs D1a and b, respectively.

The photoionization models in Fig. D1a were generated using CLOUDY for a radiation-bounded cloud with varying values of density, ionization parameter and spectral index. The measured ratios in our apertures for NGC 1068 and NGC 4151 are consistent with this grid; however, the corresponding ionization parameters are a half-an-order-of-magnitude higher than that which was required to reproduce the measured TR line ratios ($\log U = -3$; Fig. 4). This is further evidence that radiation-bounded AGN photoionization is not the dominant ionization mechanism in our apertures, and in the case of NGC 1068, it can be explained as the [O III] and Hβ emission being dominated by matter-bounded components (as

indicated by the measured He II/Hβ ratios; Fig. 5). This is because matter-bounded emission will increase the relative strength of the [O III] and Hβ lines, reducing the [O III](7319 + 7331)/[O III] $\lambda 5007$ and [S II](4068 + 4076)/Hβ ratios used in Fig. D1a and thus giving a higher corresponding ionization parameter on the radiation-bounded grid.

In Fig. D1b, we present the same measured ratios, but with the expected ratios from shock-ionization modelling. The shock models here are those presented by Allen et al. (2008) and are for two values of pre-shock density ($10^1 \, \mathrm{cm^{-3}}$ and $10^2 \, \mathrm{cm^{-3}}$), velocities of $v_{\mathrm{shock}} = 400$, 600, and $800 \, \mathrm{km \, s^{-1}}$, and magnetic parameters in the range $2 < B/\sqrt{n} < 10 \, \mu G \, \mathrm{cm^{3/2}}$. In all apertures for NGC 4151, the measured line ratios are consistent with shock ionization, albeit with relatively high magnetic parameters ($4 < B/\sqrt{n} < 10 \, \mu G \, \mathrm{cm^{3/2}}$). These magnetic parameters are higher than those typical for the ISM (($2 < B/\sqrt{n} < 4 \, \mu G \, \mathrm{cm^{3/2}}$); Dopita & Sutherland 1995; Allen et al. 2008), potentially indicating higher magnetic fields associated with the shocked material. If the gas detected in our NGC 4151 data is indeed shock-ionized, then the position of the shock model grid on the diagram would explain why the ionization parameter deduced from the radiation-bounded photoionization grid (Fig. D1a) for the NGC 4151 apertures is higher than expected from the TR diagnostic grid (Fig. 4): shock ionization produces lower values of [O II](7319 + 7331)/[O III] $\lambda 5007$ and [S II](4068 + 4076)/Hβ, corresponding to higher ionization parameters on the photoionization grid.

We also present [O II](7319 + 7331)/[O III] $\lambda 5007$ and [S II](4068 + 4076)/Hβ ratios for the Seyfert 2 galaxy IC 5063, as measured from the data set described in Holden et al. (2023). In agreement with our previous findings (Holden et al. 2023), we find that the ratios are consistent with radiation-bounded AGN-photoionization for an ionization parameter of $-3 < \log U < -2$ and densities in the range $3 < \log_{10}(n_e[\mathrm{cm^{-3}}]) < 4$.
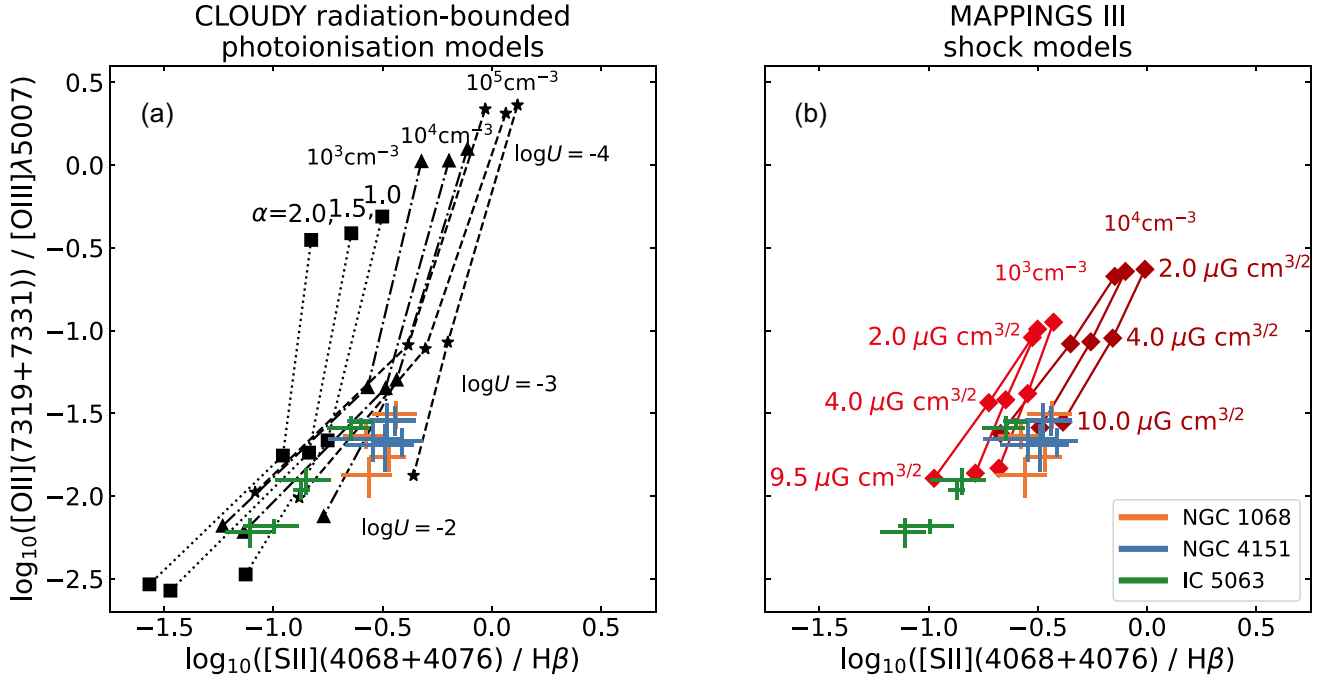
Figure D1. TR([S II])/Hβ versus TR([O II])/[O III] λ5007 ratio grids from CLOUDY radiation-bounded photoionization modelling (a) and the Allen et al. (2008) MAPPINGS III shock-ionization models (b), along with measured values for each aperture in NGC 1068 (orange crosses), NGC 4151 (blue crosses), and IC 5063 (green crosses; see Holden et al. 2023). The modelled photoionization line ratio grid shown in (a) is for three spectral indices ($\alpha = 1.0$, 1.5, and 2.0; labelled) at different electron densities (squares: $n_{\rm e} = 10^3$ cm^{-3}; triangles: 10^4 cm^{-3}; stars: 10^5 cm^{-3}) and ionization parameters (log U; labelled), while the shock-ionization grids in b) are for post-shock densities of $n = 10^3$ cm^{-3} and $n = 10^4$ cm^{-3} (labelled; assuming a shock compression factor of 100), magnetic parameters of $B/\sqrt{n} = 2$, 4, 10 μG cm$^{3/2}$. (labelled), and velocities of $v_{\rm shock} = 400$, 600, and 800 km s^{-1}.

This paper has been typeset from a TeX/LaTeX file prepared by the author.